nature cardiovascular research

Article

https://doi.org/10.1038/s44161-022-00155-0

GPR55 in B cells limits atherosclerosis development and regulates plasma cell maturation

Received: 5 January 2022

Accepted: 27 September 2022

Published online: 11 November 2022

Check for updates

Raquel Guillamat-Prats[1], Daniel Hering[1], Abhishek Derle[1], Martina Rami[1], Carmen Härdtner[2], Donato Santovito[1,3,4], Petteri Rinne[5], Laura Bindila[6], Michael Hristov[1], Sabrina Pagano[7], Nicolas Vuilleumier[7], Sofie Schmid[8], Aleksandar Janjic[9], Wolfgang Enard[9], Christian Weber[1,3,10,11], Lars Maegdefessel[3,8], Alexander Faussner[1], Ingo Hilgendorf[2,12] & Sabine Steffens[1,3]

Dissecting the pathways regulating the adaptive immune response in atherosclerosis is of particular therapeutic interest. Here we report that the lipid G-protein-coupled receptor GPR55 is highly expressed by splenic plasma cells (PCs), upregulated in mouse spleens during atherogenesis and human unstable or ruptured compared to stable plaques. *Gpr55*-deficient mice developed larger atherosclerotic plaques with increased necrotic core size compared to their corresponding controls. Lack of GPR55 hyperactivated B cells, disturbed PC maturation and resulted in IgG overproduction. B-cell-specific *Gpr55* depletion or adoptive transfer of *Gpr55*-deficient B cells was sufficient to promote plaque development and elevated IgG titers. In vitro, the endogenous GPR55 ligand lysophsophatidylinositol (LPI) enhanced PC proliferation, whereas GPR55 antagonism blocked PC maturation and increased their mitochondrial content. Collectively, these discoveries provide previously undefined evidence for GPR55 in B cells as a key modulator of the adaptive immune response in atherosclerosis.

Cardiovascular diseases related to atherosclerosis are the leading cause of death worldwide. Atherosclerosis is a chronic and multifactorial disease involving both arms of our immune system: the innate and adaptive immunity[1–3]. Recent advances in analytical approaches, such as single-cell sequencing and mass cytometry, have deepened our knowledge about the cellular heterogeneity within the atherosclerotic lesions[4], supporting the relevance of B lymphocytes in the pathophysiology of the disease.

[1]Institute for Cardiovascular Prevention (IPEK), Ludwig-Maximilians-Universität (LMU) Munich, Munich, Germany. [2]Department of Cardiology and Angiology I, Heart Center and Faculty of Medicine, University of Freiburg, Freiburg, Germany. [3]German Center for Cardiovascular Research (DZHK), Partner Site Munich Heart Alliance (MHA), Munich, Germany. [4]Institute for Genetic and Biomedical Research (IRGB), Unit of Milan, National Research Council, Milan, Italy. [5]Institute of Biomedicine, University of Turku, Turku, Finland. [6]Institute of Physiological Chemistry, University Medical Center of the Johannes Gutenberg University Mainz, Mainz, Germany. [7]Division of Laboratory Medicine, Diagnostic Department, Geneva University Hospitals and Faculty of Medicine, Geneva, Switzerland. [8]Department of Vascular and Endovascular Surgery, Klinikum rechts der Isar - Technical University Munich (TUM), Munich, Germany. [9]Anthropology and Human Genomics, Faculty of Biology, Ludwig-Maximilians-Universität (LMU), Martinsried, Germany. [10]Department of Biochemistry, Cardiovascular Research Institute Maastricht (CARIM), Maastricht University Medical Centre, Maastricht, The Netherlands. [11]Munich Cluster for Systems Neurology (SyNergy), Munich, Germany. [12]Institute for Experimental Cardiovascular Medicine, Heart Center and Faculty of Medicine, University of Freiburg, Freiburg, Germany. e-mail: sabine.steffens@med.uni-muenchen.de

Diverse subset-specific functions of B cells in atherosclerosis have been described over the last years, reporting both pro-atherogenic and anti-atherogenic properties[5–8]. For example, B1a cells are considered as main producers of naturally occurring IgM antibodies arising without antigen-mediated induction. These antibodies recognize oxidation-specific epitopes (OSEs) that are present on lipoprotein particles as well as apoptotic cells, thereby limiting atherosclerotic plaque progression[8]. The B2 lineage can be separated into marginal zone (MZ) and follicular (FO) cells. MZ cells are positioned at the splenic red pulp border to scan the blood for circulating antigens, and FO cells interact with T follicular helper (Tfh) cells to initiate the germinal center (GC) response[9]. This culminates in the final stage of B cell maturation, which involves the rapid proliferation of plasmablasts secreting low antibody levels, somatic hypermutations in the B cell receptor (BCR) region and selection of high antigen affinity clones to ultimately differentiate into long-lived PCs[10]. PCs have a high protein synthesis capacity and secrete large amounts of antibodies into the circulation, which depends on a set of transcription factors, including PR domain zinc finger protein 1 (BLIMP1), interferon regulatory factor 4 (IRF4) and X-box binding protein 1 (XBP1). Antigen-specific antibodies of various isotypes, including IgGs, are produced by class-switching of the high-affinity B cell clones.

In the context of atherosclerosis, IgGs have been reported to form immune complexes with oxidized low-density lipoprotein (oxLDL) and promote macrophage inflammatory responses[11]. High-throughput single-cell analysis of the atherosclerosis-associated antibody repertoire recently discovered atheroprotective anti-ALDH4A1 auto-antibodies directed against a mitochondrial dehydrogenase[12]. MZ B cells have been shown to negatively control pro-atherogenic Tfh responses to hypercholesterolemia[13], which underlines the complexity of B cell subset-specific functions and auto-antibodies in atherosclerosis.

B cell activation involves antigen binding to the BCRs, which are membrane-bound immunoglobulins with unique epitope-binding sites expressed by each clone. The BCRs form a signaling complex with other receptors on the B cell surface, including, among others, protein tyrosine phosphatase receptor type C (PTPRC, also known as B220)[11].

GPR55 is a G-protein-coupled orphan receptor expressed by various leukocyte subsets, including B and T cells, but also natural killer cells, monocytes, macrophages and neutrophils. According to murine immune cell transcriptomic data (https://www.immgen.org/)[14], GPR55 is highly expressed by splenic PCs and, to a lower extent, MZ B cells. The most potent endogenous GPR55 ligand identified so far is LPI[15–17], which is synthesized by the enzyme phospholipase DDHD domain containing 1 (DDHD1). Within the spleen, this enzyme is mostly expressed by conventional $CD4^+$ and $CD8^+$ dendritic cells as well as red pulp macrophages (https://www.immgen.org/)[14]. Immunological functions for GPR55 have been described, among others, in γδT cells residing in intestinal lymphoid organs, where *Gpr55* deficiency or short-term antagonist treatment protected mice from non-steroidal anti-inflammatory drug-induced increases in intestinal permeability[18].

In THP1-derived macrophages, GPR55 stimulation promoted the accumulation of oxLDL and blocked cholesterol efflux, whereas GPR55 antagonism counteracted these effects[19]. In aortic endothelial cells, antagonizing GPR55 with CID16020046 prevented oxLDL-induced inflammatory stress[20]. In vivo treatment of atherosclerosis-prone apolipoprotein E-deficient (*Apoe*$^{-/-}$) mice with CID16020046 reduced neutrophil recruitment and plaque infiltration, whereas no effects on plaque size were detectable[21]. However, the role of GPR55 in regulating adaptive B cell responses in the context of atherosclerosis has not been investigated thus far.

Using a global *Gpr55* knockout mouse model, B-cell-specific deletion and adoptive transfer experiments, we report here that GPR55 plays a pleiotropic role in the B cell compartment, which crucially affects atherosclerosis. Our findings provide further insight into the complex regulation of humoral immunity and might be of broader relevance beyond atherosclerosis, such as autoimmune disorders.

Results

Modulation and role of the GPR55–LPI axis in atherosclerosis

To address the regulation of the GPR55–LPI axis during hypercholesterolemia, we fed *Apoe*$^{-/-}$ mice with Western diet (WD) for 4 weeks or 16 weeks, respectively, and measured LPI plasma levels by liquid chromatography–tandem mass spectrometry. Circulating LPI was elevated during the early stage of atherogenesis and returned to baseline concentrations after 16 weeks of WD (Fig. 1a). Given that GPR55 is highly expressed by splenic B cells, we focused on the spleen to assess a modulation of the receptor and the LPI-synthesizing enzyme DDHD1 during atherosclerosis onset and progression. In accordance with the modulation of plasma LPI levels, *Ddhd1* was upregulated after 4 weeks, but not 16 weeks, of WD (Fig. 1b). A similar pattern for the splenic *Gpr55* mRNA expression was observed (Fig. 1c). At the 4-week timepoint, the splenic GPR55 expression inversely correlated with aortic root atherosclerotic plaque size (Fig. 1d), suggesting that GPR55 signaling may exert an early protective effect on plaque development. The causal implication of GPR55 in atherogenesis was substantiated in *Apoe*$^{-/-}$*Gpr55*$^{-/-}$ mice receiving 4 weeks of WD, which developed larger plaques within aortic roots compared to corresponding *Apoe*$^{-/-}$ controls (Fig. 1e–g). These findings suggest that GPR55 signaling counterbalances plaque development, at least in early disease stage. To address the question if *Gpr55* deficiency may affect LPI levels, we compared splenic transcript levels of the LPI-producing enzyme *Ddhd1* between *Apoe*$^{-/-}$ and *Apoe*$^{-/-}$*Gpr55*$^{-/-}$ mice and detected higher levels in *Gpr55*-deficient mice. Nevertheless, the relative expression levels followed a similar pattern over the course of atherogenic diet feeding, as observed in *Apoe*$^{-/-}$ mice (Fig. 1h). After 10 weeks of WD, the plaque burden was higher in the descending aorta in *Apoe*$^{-/-}$*Gpr55*$^{-/-}$ mice compared to *Apoe*$^{-/-}$ mice (Extended Data Fig. 1a). After 16 weeks of WD, a more in-depth characterization of the plaque development revealed that the difference in aortic lesion area was no longer observed at this advanced stage (Extended Data Fig. 1b). In the descending aorta, however, the plaque burden was still higher in *Apoe*$^{-/-}$*Gpr55*$^{-/-}$ mice (Extended Data Fig. 1c). This might reflect stage-dependent effects of GPR55 during atherosclerosis, because plaque development in descending aortas is generally less advanced compared to aortic root plaques in mouse models of atherosclerosis[22]. In support of this hypothesis, 16-week plaques of *Gpr55*-deficient mice exhibited an increased necrotic core and collagen area but decreased relative plaque content of macrophages and lipids, indicative of a more advanced plaque phenotype (Extended Data Fig. 1d–g). These effects of *Gpr55* deficiency on the advanced plaque phenotype support a possible relevance for complications in human atherosclerosis pathophysiology.

To validate the expression and possible modulation of GPR55 in human plaques, we analyzed the transcript levels in stable and unstable carotid artery plaques collected from patients undergoing endarterectomy. The plaque phenotype was assigned based on the morphology following the American Heart Association (AHA) classification[23] with or without a vulnerable fibrous cap according to Redgrave et al.[24] (Fig. 1i and Extended Data Table 1, patient characteristics). The quantitative polymerase chain reaction (qPCR) analysis revealed reduced *GPR55* expression in unstable compared to stable plaques (Fig. 1j), which might suggest that high expression levels of this receptor may counterbalance the patient's risk for developing an acute cardiovascular event.

B cell *Gpr55* expression and functionality

We next assessed the expression profile of *Gpr55* in sorted murine blood leukocytes of *Apoe*$^{-/-}$ mice by digital droplet PCR (ddPCR) and qPCR. The rank order of *Gpr55* expression in the different populations was B cells > T cells > neutrophils > monocytes, which was consistently confirmed by both techniques (Fig. 2a). Moreover, we determined *Gpr55* expression in different B cell subsets, which confirmed a higher expression in PCs compared to GC B cells, followed by B2 and B1 subsets (Fig. 2a). By in situ hybridization, we localized *Gpr55* expression in the splenic B cell FO and GC areas (Fig. 2b).

https://doi.org/10.1038/s44161-022-00155-0

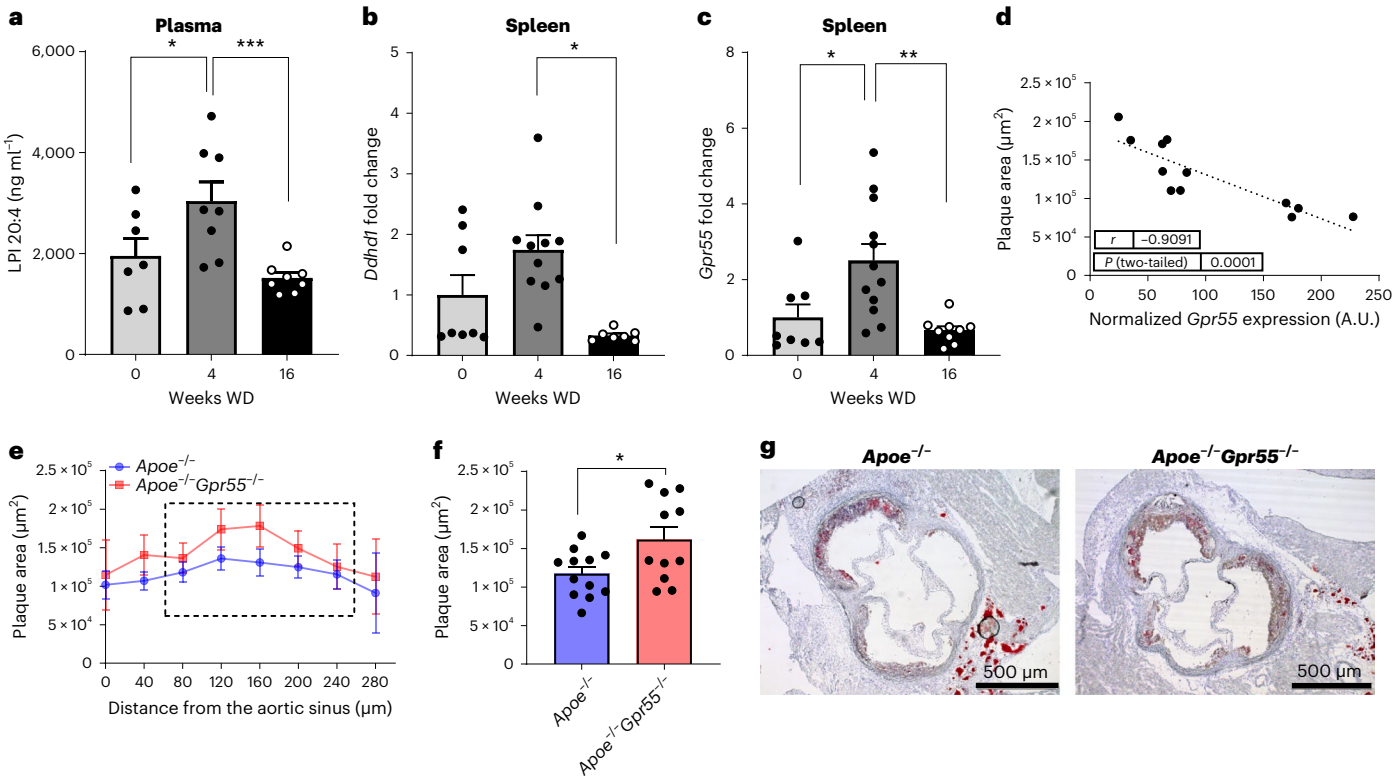

Fig. 1 | Regulation and function of GPR55 signaling in atherosclerosis. **a**–**d**, Plasma, spleens and aortic roots were collected from *Apoe*$^{-/-}$ mice at baseline or after 4 weeks and 16 weeks of WD to determine LPI plasma concentrations ($n = 7$–8; $^*P = 0.05$ and $^{***}P = 0.0042$) (**a**) or relative splenic mRNA expression of the gene encoding the LPI-synthesizing enzyme DDHD1 ($n = 7$–11; $P = 0.0018$) and the LPI receptor GPR55 ($n = 7$–12; $^*P = 0.019$ and $^{**}P = 0.0028$) (**b**,**c**). **d**, Splenic *Gpr55* mRNA expression values of the 4-week timepoint were plotted against the aortic root plaque areas of the same mice ($n = 12$). **e**, Plaque area per aortic root section of female *Apoe*$^{-/-}$ and *Apoe*$^{-/-}$*Gpr55*$^{-/-}$ mice after 4 weeks of WD ($n = 11$–12 per group; $^*P = 0.023$). The dotted square indicates the sections used for calculating the average plaque area per animal shown in **f**. **g**, Representative Oil Red O stains of aortic roots after 4 weeks of WD. **h**, Splenic *Ddhd1* mRNA expression of baseline, 4 weeks and 16 weeks WD *Apoe*$^{-/-}$ and *Apoe*$^{-/-}$*Gpr55*$^{-/-}$ mice (for baseline $n = 7$–9; for 4 weeks $n = 6$–8 and $^*P = 0.04$; and for 16 weeks $n = 6$–7 and $^*P = 0.035$). **i**, Representative pictures of human stable and unstable plaques (obtained from the Munich Vascular Biobank; shown is one of the eight samples evaluated). **j**, Human *GPR55* mRNA expression evaluated by qPCR in stable versus unstable/ruptured carotid artery plaque corrected by *RPLPO* used as housekeeping control ($^{***}P = 0.0006$). The box plot shows the minimum to maximum value, and each dot represents one patient. Mouse data shown in **a**–**f** were combined from three independent experiments. Each dot represents one biologically independent mouse sample. All data are shown as mean ± s.e.m. Two-sided unpaired Student's *t*-test or one-way ANOVA followed by post hoc Newman–Keuls multiple comparison test was used to determine the significant differences. Bivariate correlation was analyzed by Spearman's rank correlation test. A.U., arbitrary units; FC, fibrous cap; M, media; NC, necrotic core.

The functional GPR55 signaling response in B cells was subsequently validated by measuring intracellular calcium (Ca^{2+}) increases in response to stimulation with the endogenous GPR55 ligand LPI. We tested a soybean extract with a mix of different LPI species and pure 20:4 LPI, the specific ligand for GPR55, in circulating B cells of *Apoe*$^{-/-}$ mice, both in normal diet condition and hypercholesterolemia after 10 weeks of WD, as well as circulating B cells of WT mice under normal diet condition. Independent of the genetic background or diet, similar baseline intracellular Ca^{2+} levels and similar responses to soybean LPI and 20:40 LPI were observed (Fig. 2c). Therefore, subsequent in vitro and in vivo experiments were performed only with the soybean LPI mix. When comparing *Apoe*$^{-/-}$ and *Apoe*$^{-/-}$*Gpr55*$^{-/-}$ B cell responses in normal diet condition, an increase in intracellular Ca^{2+} after LPI stimulation was observed only in *Gpr55*-expressing *Apoe*$^{-/-}$ cells (Fig. 2d). *Gpr55*

deficiency did not affect basal intracellular Ca^{2+} levels, and treatment with the potent B cell stimulus anti-IgM[25,26] resulted in similarly strong Ca^{2+} responses, suggesting that BCR activation by GPR55-independent signals is not compromised in absence of the receptor. Furthermore, human peripheral blood B cells showed a dose-dependent Ca^{2+} response to LPI, indicating a functional LPI-GPR55 signaling pathway in human B cells (Fig. 2e,f).

Gpr55 deficiency disturbs metabolism and drives inflammation

Apoe$^{-/-}$*Gpr55*$^{-/-}$ mice had pronounced metabolic changes, in particular increased body weight compared to aged-matched *Apoe*$^{-/-}$ animals, which was already notable at baseline and consistently evident after 4 weeks, 10 weeks or 16 weeks of WD (Extended Data Fig. 2a–c). Although plasma cholesterol levels were not significantly different compared to *Apoe*$^{-/-}$ controls at all timepoints (Extended Data Fig. 2d), the lipoprotein profile analysis at the 4-week timepoint showed larger very-low-density lipoprotein (VLDL) and LDL fractions in *Apoe*$^{-/-}$*Gpr55*$^{-/-}$ mice (Extended Data Fig. 2e). Likewise, the liver total cholesterol was not significantly altered after 4 weeks of WD ($P = 0.086$; Extended Data Fig. 2f). Nevertheless, the hepatic qPCR gene expression analysis at the same timepoint revealed a significant transcriptional upregulation of several metabolic markers, indicating enhanced lipid synthesis, uptake and efflux in *Apoe*$^{-/-}$*Gpr55*$^{-/-}$ mice (Extended Data Fig. 2g). Furthermore, the Oil Red O staining analysis of liver sections revealed an enhanced lipid droplet accumulation after 16 weeks of WD (Extended Data Fig. 2h,i).

We next investigated the effect of global GPR55 deficiency on vascular and systemic inflammation under conditions of hypercholesterolemia. Compared to *Apoe*$^{-/-}$ controls, *Apoe*$^{-/-}$*Gpr55*$^{-/-}$ mice had a hyper-inflammatory phenotype with an increase in all major circulating and aortic leukocyte subsets (Extended Data Fig. 2j–l), accompanied by an amplified aortic gene expression profile of key pro-inflammatory markers (Extended Data Fig. 2m). Similar effects on plaque development and metabolic changes, as detailed in female mice, were observed in male *Apoe*$^{-/-}$*Gpr55*$^{-/-}$ mice (Extended Data Fig. 3a–c).

Gpr55 deficiency triggers antibody responses

To seek for a possible underlying reason for the excessive pro-inflammatory phenotype and considering that GPR55 is highly expressed by splenic B cells (Fig. 2a), we performed a detailed flow cytometric profiling of B cell populations (Extended Data Fig. 4). Because splenic GPR55 expression was upregulated after 4 weeks of WD but not at the later stage (Fig. 1c), we subsequently focused on this timepoint for an in-depth profiling of the *Gpr55*-deficient B cell phenotype. The flow cytometric analysis showed a diminished number of splenic B1a counts in *Apoe*$^{-/-}$*Gpr55*$^{-/-}$ mice compared to *Apoe*$^{-/-}$ controls, whereas B2 MZ cell counts were increased (Fig. 3a). The most pronounced changes were reductions of splenic GC B cell and PC counts in *Apoe*$^{-/-}$*Gpr55*$^{-/-}$ mice (Fig. 3a). A similar pattern was observed when comparing the relative frequencies among splenic B cell subsets (Fig. 3be). B1 cells in *Apoe*$^{-/-}$*Gpr55*$^{-/-}$ mice were shifted to a decreased proportion of the anti-atherogenic B1a subset with increased B1b subset (Fig. 3b,c). Furthermore, there was a decreased proportion of the FO subset and increased proportion of the pro-atherogenic MZ subset (Fig. 3d,e). These flow cytometric data were supported by immunohistological analysis of splenic tissue sections, indicating that B cell FO and GC areas were less well-defined in mice lacking a functional GPR55 receptor (Fig. 3f).

Despite the reduced splenic PC counts, *Apoe*$^{-/-}$*Gpr55*$^{-/-}$ mice had elevated titers of IgA antibodies and several IgG subclasses (Fig. 3g). The most pronounced increase was detected in IgG2c antibody titers. Similar increases of IgG subclass titers were observed in male *Apoe*$^{-/-}$*Gpr55*$^{-/-}$ mice (Extended Data Fig. 3d). In support of the hypothesis that IgG might play a major causal role in the pro-atherogenic phenotype in absence of GPR55, we found a clear positive correlation between IgG titers and plaque size in *Apoe*$^{-/-}$*Gpr55*$^{-/-}$ mice after 4 weeks of WD (Fig. 3h). IgG titers were still higher in *Apoe*$^{-/-}$*Gpr55*$^{-/-}$ mice after 10 weeks and 16 weeks of WD, showing that the phenotype was sustained at advanced stages of atherosclerosis (Fig. 3i,j). To clarify whether *Gpr55* deficiency per se affected B cell maturation and antibody secretion, independent of antigens such as OSE arising during hypercholesterolemia, we also quantified antibody titers in the plasma of young mice at 4 weeks of age just after weaning. No differences in antibody titers between young *Apoe*$^{-/-}$ and *Apoe*$^{-/-}$*Gpr55*$^{-/-}$ were detectable, suggesting that an increase of circulating auto-antigens during the first weeks of age, likely promoted by pro-atherogenic conditions, promotes the hyperactivated phenotype of B cells when functional GPR55 signaling is lacking (Fig. 3k). Moreover, *Apoe*$^{-/-}$*Gpr55*$^{-/-}$ mice under WD had elevated plasma levels of B cell activating factor (BAFF; Fig. 3l), which is crucial for B cell survival, altogether indicating a hyperactivated B cell response during atherosclerosis in the absence of GPR55 signaling.

The hyperactivated B cell state was linked to an increased number of splenic Tfh cells and circulating plasmablasts in *Apoe*$^{-/-}$*Gpr55*$^{-/-}$ mice (Fig. 3m,n), whereas long-lived PC counts in the bone marrow were unchanged (Fig. 3o). Taken together, these data suggest an unbalanced humoral response in atherosclerotic mice lacking functional GPR55 signaling, possibly due to disturbed checkpoints controlling the B cell differentiation from a highly proliferative into a specialized antibody-secreting cell.

To clarify whether the changes in splenic B2 subsets in absence of functional GPR55 signaling may reflect a defect in B cell maturation, we assessed the lymphoid and B cell progenitor counts of *Apoe*$^{-/-}$*Gpr55*$^{-/-}$ mice after 4 weeks of WD compared to corresponding *Apoe*$^{-/-}$ controls. *Apoe*$^{-/-}$*Gpr55*$^{-/-}$ mice had lower numbers of immature B cells in the bone marrow and a decrease in the pro-B and activated B cell populations in the spleen, suggesting that GPR55 has an impact at early stages of B cell differentiation (Fig. 3p,q).

Similar changes in the splenic B cell compartment were observed in female *Gpr55*$^{-/-}$ mice on wild-type (WT) background without *Apoe*$^{-/-}$ deficiency, with increased numbers of B2 MZ B cells and a reduction of PCs (Extended Data Fig. 5a–f). These mice also had increased IgG titers (Extended Data Fig. 5b), accompanied by a decrease in bone marrow long-lived PCs, whereas circulating plasmablast counts were not significantly different (Extended Data Fig. 5e,f). These data suggest that *Gpr55* deficiency per se affects humoral B cell responses even in absence of hypercholesterolemic conditions, even though the phenotype is more pronounced on *Apoe*$^{-/-}$ background combined with atherogenic diet feeding.

Chronic LPI administration does not affect atherogenesis

Next, we asked if the observed in vitro effects of LPI on PC maturation could be reproduced in vivo by injecting exogenous LPI and whether

Fig. 2 | GPR55 expression and Ca^{2+} responses in murine and human B cells. **a**, *Gpr55* mRNA expression determined by ddPCR (left) and qPCR (right) in sorted circulating leukocyte subsets and splenic B cell subsets. Each dot represents sorted cells from an individual *Apoe*$^{-/-}$ mouse ($n = 3–4$). **b**, In situ hybridization to detect *Gpr55* (red) in splenic GC areas (PNA^+, green; nuclei, blue). The assay was performed with three independent *Apoe*$^{-/-}$ mouse samples. **c**, Average MFI of intracellular Ca^{2+} sensor in circulating B cells of *Apoe*$^{-/-}$ mice under normal diet (baseline) or 10 weeks of WD and C57BL/6J WT mice under normal diet, in response to soybean LPI or pure 20:4 LPI stimulation ($n = 4$). **d**, Average MFI of intracellular Ca^{2+} sensor in circulating B cells of *Apoe*$^{-/-}$ and *Apoe*$^{-/-}$*Gpr55*$^{-/-}$ mice in response to LPI or anti-IgM stimulation ($n = 4–8$). Representative histogram (**e**) and average MFI (**f**) of intracellular Ca^{2+} sensor in human B cells at baseline conditions and after addition of vehicle or LPI. Data were combined from two independent experiments, and each dot represents one biologically independent mouse or human sample ($n = 7–8$). All data are shown as mean ± s.e.m. One-way ANOVA followed by a post hoc Newman–Keuls multiple comparison or two-way ANOVA followed by a Kruskal–Wallis test with Dunn post hoc test was used to evaluate the significant differences. w, weeks.

https://doi.org/10.1038/s44161-022-00155-0

it may affect atherogenesis. We used a daily dose of 0.1 mg kg^{-1} based on previously reported in vivo doses for testing the effect of LPI injection on liver steatosis[27], which was in the range of the plasma LPI levels measured in our *Apoe*$^{-/-}$ model. Daily intraperitoneal (i.p.) administration of LPI for 4 weeks in parallel to the atherogenic diet affected neither the plaque size nor circulating antibody titers, B cell counts and splenic B cells. Only a slight, yet significant, increase in plasma cholesterol compared to the vehicle group was observed (Extended Data Fig. 6). Although we cannot exclude that the LPI dose was insufficient to affect splenic PC responses and plaque development, or possibly

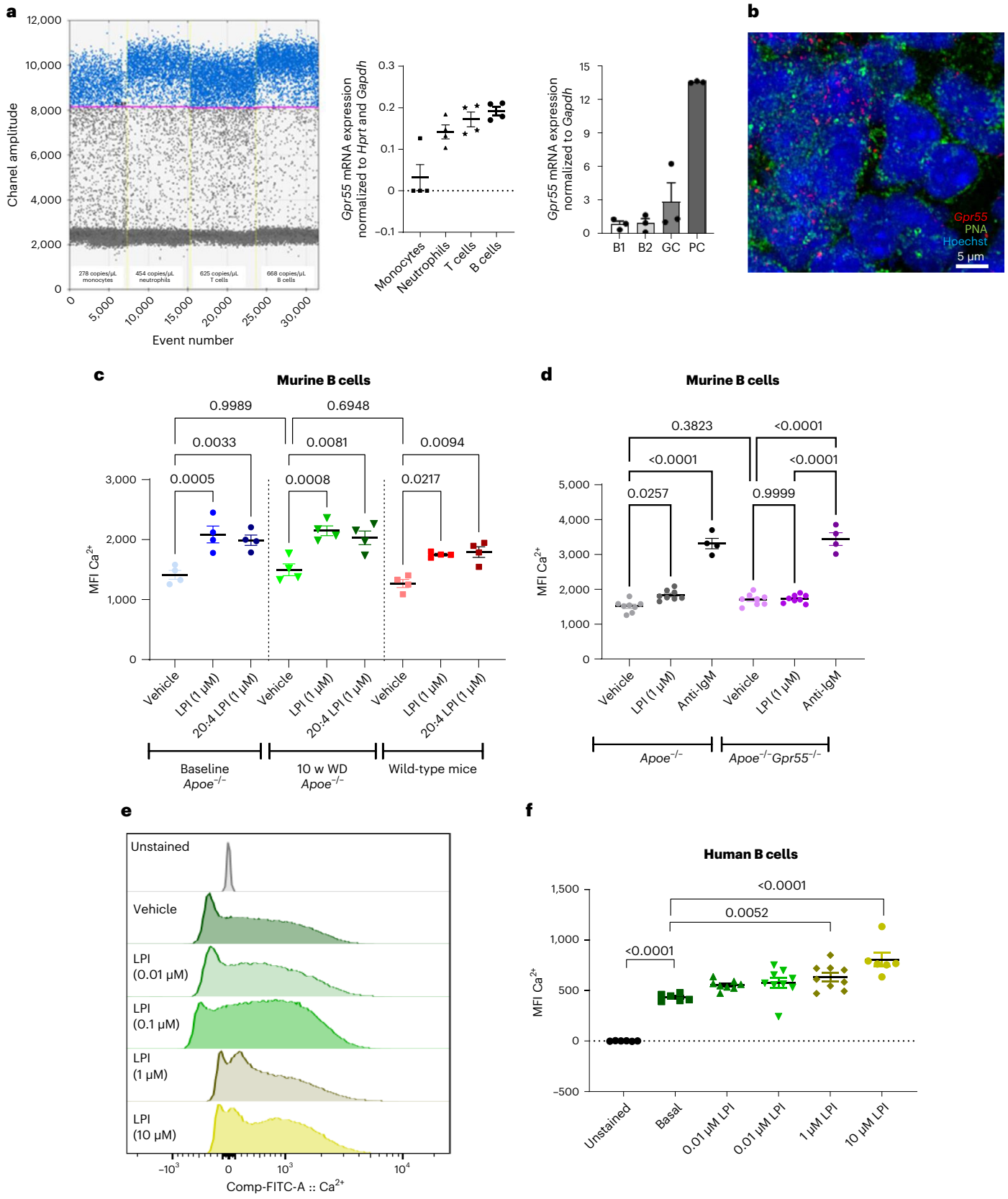

https://doi.org/10.1038/s44161-022-00155-0

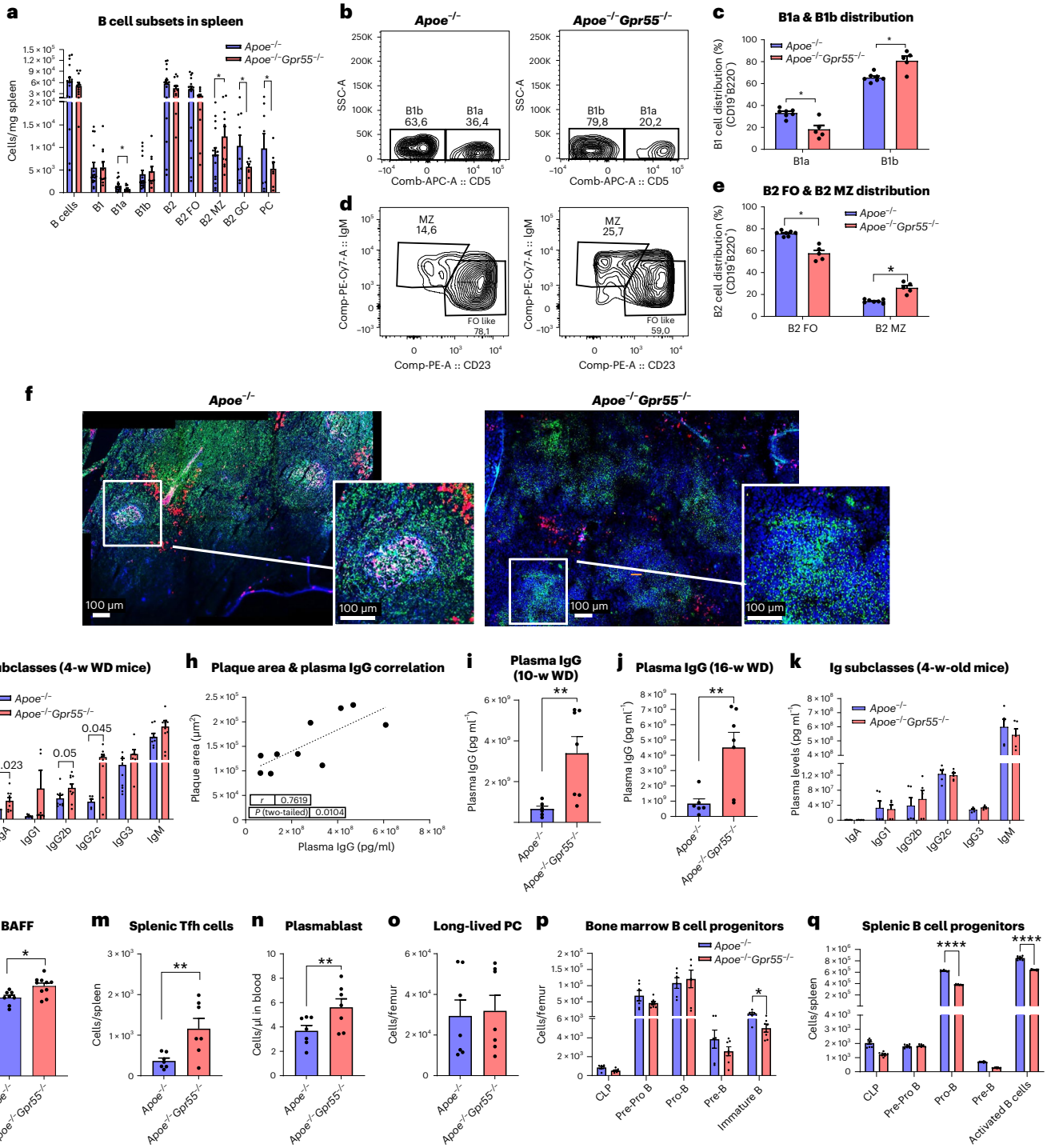

Fig. 3 | B cell immunoprofiling of global *Gpr55*-deficient mice after 4 weeks of WD. a, Splenic B cell subsets quantified by flow cytometry ($n = 15–16$; $^*P < 0.05$). **b**,**c**, Representative gating strategy and relative proportion of B1 cell subsets. **d**,**e**, Representative gating strategy and relative proportion of B2 cell subsets ($n = 5–7$; $^*P < 0.05$). **f**, Confocal imaging of spleen sections stained for B cell markers PNA (GC, green), IgM (MZ or memory B cells, red), CD23 (FO B cells, pink) and nuclei (blue). Six independent samples were analyzed. Plasma Ig titers ($n = 6–9$) (**g**) and IgG titers ($n = 10$) (**h**) plotted against aortic plaque size in *Gpr55*-deficient mice. Plasma IgG titers in mice after 10 weeks of WD ($n = 6–7$; $^*P = 0.0047$) (**i**) or 16 weeks of WD ($n = 6–7$; $^*P = 0.0045$) (**j**). **k**, Plasma Ig titers in young 4-week-old mice ($n = 5$). **l**, BAFF concentrations after 4 weeks of WD ($n = 8$-10; $^{**}P = 0.0098$). Number of splenic Tfh cells ($n = 7$; $^{**}P = 0.010$) (**m**), circulating plasmablasts ($n = 7$; $^{**}P = 0.035$) (**n**) and long-lived PCs in bone marrow (**o**) assessed by flow cytometry after 4 weeks of WD. Lymphoid B cell progenitors in the bone marrow ($n = 5–7$; $^*P < 0.05$) (**p**) and spleen ($n = 5–7$; $^{****}P = 0.0001$) (**q**) after 4 weeks of WD. Data were combined from two independent experiments for all figure panels, and each dot represents one biologically independent mouse sample (mean ± s.e.m.). Two-sided unpaired Student's *t*-test was used to determine the significant differences. w, weeks.

counterbalanced by pro-steatotic effects of LPI[27], another explanation could be that LPI might not be the only endogenous ligand affecting GPR55 signaling in vivo.

Bulk RNA sequencing analysis of splenic B cells

To understand in more detail the role of GPR55 signaling in splenic B cells, we sorted splenic CD19$^+$ B cells from six *Apoe*$^{-/-}$ and six

Apoe$^{-/-}$*Gpr55*$^{-/-}$ mice after 4 weeks of WD and performed prime-seq, a bulk RNA sequencing protocol[28]. We found 460 differentially expressed genes (DEGs) between *Apoe*$^{-/-}$ and *Apoe*$^{-/-}$*Gpr55*$^{-/-}$ mice that were enriched in B and T cell activation, cellular response to stress and intracellular signal transduction (Fig. 4a and Extended Data Fig. 7a,b). The main DEGs associated with each Gene Ontology (GO) pathway were validated by qPCR, confirming a decrease of *Fcer2a*/CD23 and *Ptprc*/LPAP in *Apoe*$^{-/-}$*Gpr55*$^{-/-}$ B cells, together with changes in *Zbtb20*, *Xbp1* and *Bcl6*, which are important transcription factors involved in B cell maturation and PC differentiation (Fig. 4b)[11]. To study in more depth the transcriptomic changes linked to altered PC maturation in *Gpr55*-deficient mice, we also performed bulk RNA sequencing of sorted splenic PCs, blood plasmablasts and bone marrow long-lived PCs from *Apoe*$^{-/-}$ versus *Apoe*$^{-/-}$*Gpr55*$^{-/-}$ mice. The integration of differentially regulated GO pathways in a chord diagram confirmed that the three populations show overlapping regulated pathways, such as B and T cell activation, disrupted Ig production and activated cell stress genes, confirming that B cell maturation and PC function is generally affected by G*pr55* deficiency (Fig. 4c). To further explore the underlying mechanisms caused by the lack of GPR55 signaling, we performed gene set enrichment analysis (GSEA) to identify the immunological molecular signatures altered in our *Apoe*$^{-/-}$*Gpr55*$^{-/-}$ B cell gene set. We found that *Gpr55* deficiency in B cells was linked to an increased expression of genes necessary for antigen-specific and neutralizing antibody production, supporting the hypothesis that GPR55 in B cells is necessary to control antibody production (false discovery rate (FDR) $q = 0.0029$). Accordingly, *Apoe*$^{-/-}$*Gpr55*$^{-/-}$ B cells downregulated genes negatively involved in antibody production (FDR $q = 0.025$). Lack of GPR55 was also associated with a downregulation of genes linked to naive B cell activation and migration into the light and dark zones of the GCs, where B cell clonal expansion, hypermutation and selection of high-affinity antibody-secreting PCs occurs (FDR $q = 0.0234$). In addition, *Apoe*$^{-/-}$*Gpr55*$^{-/-}$ B cells downregulated genes involved in pre-B cell differentiation, signifying that B cell maturation might be affected by *Gpr55* deficiency (FDR $q = 0.0410$) (Extended Data Fig. 7c).

In *Apoe*$^{-/-}$ controls, the total splenic G*pr55* expression directly correlated with *Fcer2a*/CD23 and *Ptcarp*/LPAP (Fig. 4d,e). B2 FO cells downregulate *Fcer2a*/CD23 expression on the cell surface when they go into memory B cell differentiation[29]. *Ptprc*/LPAP expression was lower in *Apoe*$^{-/-}$*Gpr55*$^{-/-}$ mice, which is in line with previous data reporting that LPAP deficiency is associated with increased MZ B2 cell numbers[30]. Evaluation of transcriptional factors involved in B cell biology revealed lower expression of *Zbtb20* in spleens of *Apoe*$^{-/-}$*Gpr55*$^{-/-}$ mice, whereas *Xbp1* expression was two-fold increased (Fig. 4b). *Zbtb20* is a key player in late B cell differentiation and is highly expressed by GC B cells and PCs[31]. The decreased levels in *Apoe*$^{-/-}$*Gpr55*$^{-/-}$ mice are in line with the lower numbers of GC B cells and disturbed PC differentiation (Fig. 3a)[31]. Overexpression of *Xbp1* promotes long-lived PC differentiation and is crucial for switching into secretory cells, releasing large quantities of antibodies and inducing endoplasmic reticulum (ER) remodeling, autophagic pathways and the unfolded protein response (UPR)[32]. Ex vivo stimulation of splenocytes with the GPR55 agonist LPI upregulated CD23 surface expression levels in B cells, with a maximum effect observed after 30 minutes (Fig. 4f). To substantiate these findings, we compared the CD23 protein expression on splenic B cell subsets after 4 weeks of atherogenic diet, confirming reduced surface expression in the total CD19^{+} and B2 population and, in particular, B2 FO cells of *Apoe*$^{-/-}$*Gpr55*$^{-/-}$ mice (Fig. 4g).

To further study the role of GPR55 in PC differentiation, we performed additional in vitro experiments. Splenic B cells isolated from *Apoe*$^{-/-}$ and *Apoe*$^{-/-}$*Gpr55*$^{-/-}$ mice were stimulated with a cocktail of LPS, IFN-α, IL2, IL4 and IL5 for 72 hours to trigger PC differentiation alone or in the presence of the GPR55 agonist LPI or the antagonist CID16020046, respectively. Co-incubation with LPI resulted in more differentiated PCs compared to cells treated with LPS/IFN-α/IL2/IL4/IL5 alone in B cells isolated from *Apoe*$^{-/-}$ mice, whereas adding the GPR55 antagonist prevented the LPS/IFN-α/IL2/IL4/IL5-induced induction of PC differentiation (Extended Data Fig. 8a). The effect observed with the GPR55 antagonist without addition of exogenous ligand suggests that pro-inflammatory stimulation leads to endogenous GPR55 ligand production in splenic B cells, which triggers an autocrine receptor activation. The number of differentiated plasmablasts after stimulation with the cytokine cocktail was similar between *Apoe*$^{-/-}$ and *Apoe*$^{-/-}$*Gpr55*$^{-/-}$ B cells. As expected, neither LPI nor GPR55 antagonism affected the cytokine-induced plasmablast counts in *Apoe*$^{-/-}$*Gpr55*$^{-/-}$ cells.

In addition, GPR55 antagonism or genetic depletion significantly augmented the mitochondrial content of in vitro differentiated PCs, which may reflect enhanced antibody secretion and cell stress (Extended Data Fig. 8b). We subsequently performed confocal/stimulated emission depletion (STED) imaging of unstimulated splenic PCs freshly sorted from *Apoe*$^{-/-}$ and *Apoe*$^{-/-}$*Gpr55*$^{-/-}$ mice, which uncovered a different morphology in *Apoe*$^{-/-}$*Gpr55*$^{-/-}$ cells, with enlarged, fused mitochondria and modified actin cytoskeleton (Extended Data Fig. 8c and Supplementary Videos).

Furthermore, we used flow cytometry to compare the mitochondrial content of splenic GC B cells, PCs and bone marrow long-lived PCs between *Apoe*$^{-/-}$ and *Apoe*$^{-/-}$*GPR55*$^{-/-}$ mice, which confirmed an increased mitochondrial content in all these subsets (Fig. 4h–j). We may speculate that disturbed Ca^{2+} signaling due to the lack of GPR55 leads to ER stress and increased mitochondrial content[33]. In summary, our findings support a crucial requirement for GPR55 signaling in regulating B cell activation and differentiation into PCs.

B-cell-specific *Gpr55* deficiency promotes atherosclerosis

To further address the specific contribution of B cell GPR55 signaling in atherosclerosis, we subsequently used a mixed bone marrow transplantation strategy, employing *μMT* as a model for mice lacking functional B cells, *Gpr55*$^{-/-}$ bone marrow donors on WT background and *Ldlr*$^{-/-}$ mice as recipients. *Gpr55*$^{-/-}$ bone marrow was mixed with *μMT* bone marrow in a 50/50 ratio before transplantation into lethally irradiated *Ldlr*$^{-/-}$ recipients (Fig. 5a). The B-cell-specific deficiency was validated after 6 weeks of recovery by qPCR of sorted circulating B cells,

Fig. 4 | Impact of global *GPR55* deficiency on B cell transcriptome and mitochondrial content. a, Volcano plot of DEGs in *Apoe*$^{-/-}$*Gpr55*$^{-/-}$ versus *Apoe*$^{-/-}$ splenic CD19^{+} cells after 4 weeks of WD. The *x*-axis shows $\log_2$ fold changes between genotypes. The *y*-axis plots negative $\log_{10}$ *P* values computed by DEseq2 (based on a generalized linear model) and corrected for multiple comparisons according to the Benjamini–Hochberg FDR; relevant statistically upregulated (blue) and downregulated (red) genes are highlighted ($n = 6$). **b**, Confirmation of the main DEGs in splenic B cells of *Apoe*$^{-/-}$*Gpr55*$^{-/-}$ compared to *Apoe*$^{-/-}$ mice after 4 weeks of WD by qPCR ($n = 5$; $P = 0.05$). **c**, Chord diagram showing the main regulated genes and pathways in splenic *Apoe*$^{-/-}$*Gpr55*$^{-/-}$ versus *Apoe*$^{-/-}$ B cells, splenic PCs and circulatory plasmablasts, based on RNA sequencing. Splenic B cell *Gpr55* mRNA expression (qPCR) correlated with *Fcer2a* (CD23 encoding gene) mRNA expression (**d**) and splenic B cell *Gpr55* mRNA expression (qPCR) correlated with *Ptcarpc* (LPAP encoding gene) mRNA expression (**e**) ($n = 20$ *Apoe*$^{-/-}$ mice). **f**, MFI of CD23 on splenic *Apoe*$^{-/-}$ B cells measured by flow cytometry after LPI treatment (1 μM; $n = 4$). **g**, Flow cytometric analysis of CD23 MFI on splenic B cell subsets of *Apoe*$^{-/-}$ and *Apoe*$^{-/-}$*Gpr55*$^{-/-}$ mice after 4 weeks of WD ($n = 8$–10; $^{***}P < 0.0001$). **h**, Mitochondrial content of splenic GC B cells ($n = 6$–7; $^{***}P < 0.0001$). **i**, Mitochondrial content of splenic PCs ($n = 6$–7; $^{***}P < 0.0001$). **j**, Mitochondrial content of bone marrow long-lived PCs ($n = 6$–7; $^{***}P < 0.001$). Data shown in **d**–**j** were combined from two independent experiments, and each dot represents one biologically independent mouse sample for all figure panels (mean ± s.e.m.). Two-sided unpaired Student's *t*-test or one-way ANOVA followed by a post hoc Newman–Keuls multiple comparison test was used to determine the significant differences. Bivariate correlations were analyzed by Spearman's rank correlation test. A.U., arbitrary units.

https://doi.org/10.1038/s44161-022-00155-0

whereas T cells and myeloid cells exhibited normal expression levels of *Gpr55* (Fig. 5b). At the endpoint after recovery and 10 weeks of WD feeding, the metabolic effects observed in *Apoe*$^{-/-}$*Gpr55*$^{-/-}$ mice were lost, as we did not observe changes in body weight between groups. We even observed a slightly decreased plasma cholesterol in B-cell-specific *Gpr55*-deficient mice compared to their respective controls (Fig. 5c,d).

Mice with B-cell-specific *GPR55* deficiency developed larger plaques compared to control mice transplanted with a mixture of WT/*μMT* bone marrow (Fig. 5e,f) and had fewer splenic B1 cells, MZ B cells and FO B2 cells, whereas PC counts were elevated (Fig. 5g). The distinct profile in splenic B cell subsets of B-cell-specific *Gpr55*-deficient mice compared to global *Apoe*$^{-/-}$*Gpr55*$^{-/-}$ mice indicates that

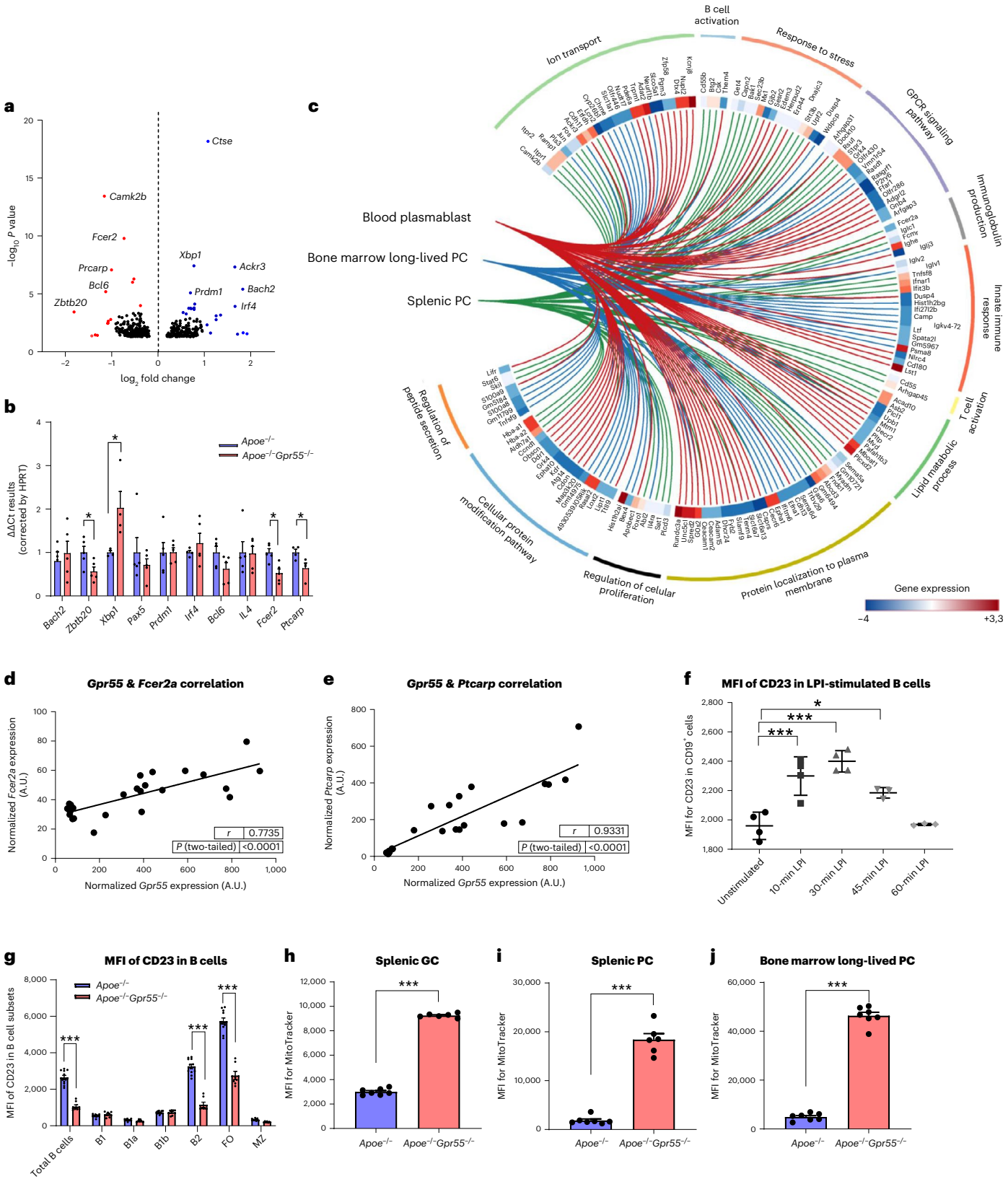

https://doi.org/10.1038/s44161-022-00155-0

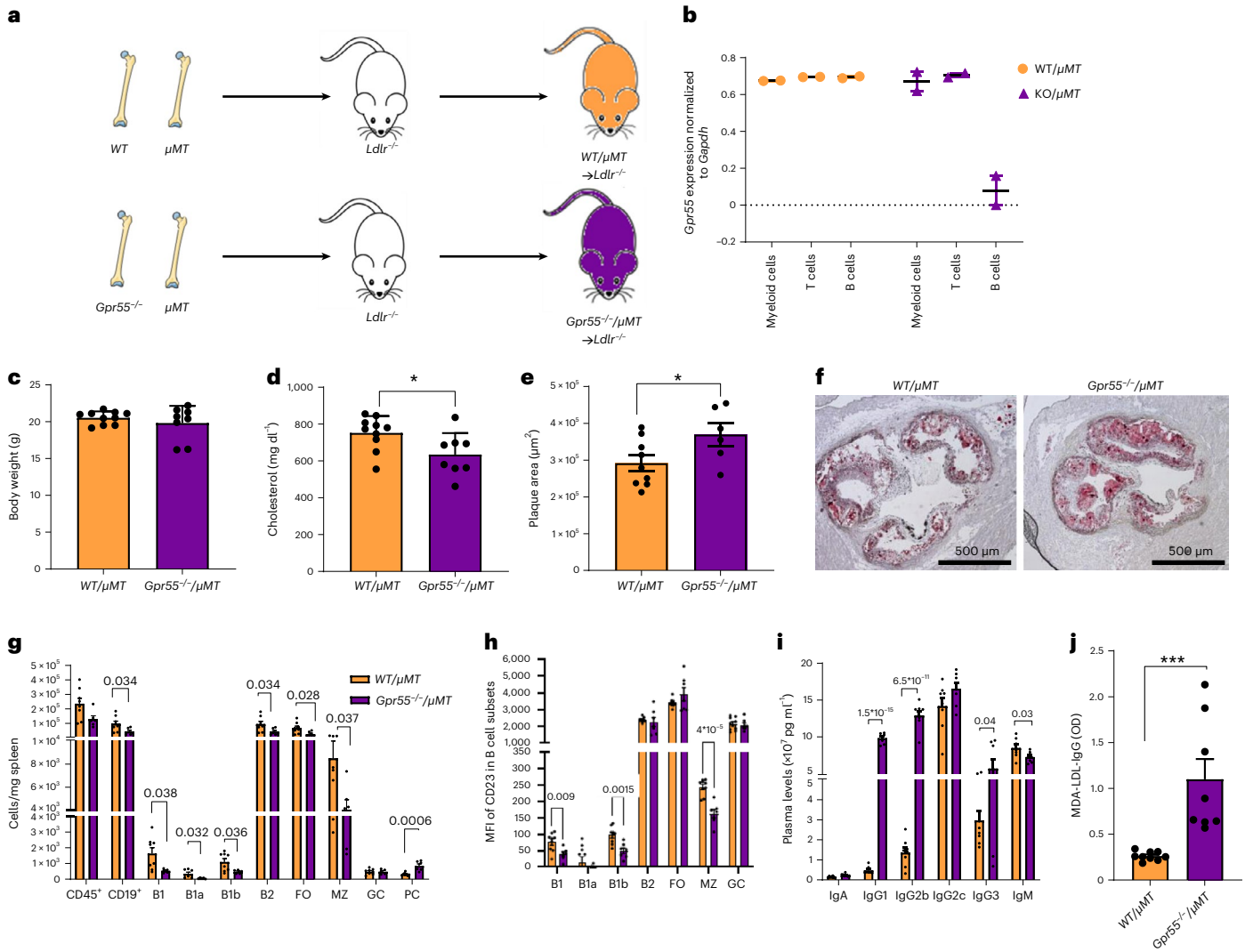

Fig. 5 | Impact of B-cell-specific *Gpr55* deficiency on atherosclerotic plaque development and B cell responses during hypercholesterolemia. **a**, Experimental design of the bone marrow transplantation to generate mixed bone marrow chimeras with B-cell-specific *Gpr55* deficiency. Lethally irradiated *Ldlr*$^{-/-}$ mice received a 50/50 mixture of *μMT* marrow and *Gpr55*$^{-/-}$ or WT marrow cells. **b**, After 6 weeks of recovery after the bone marrow transplantation, *Gpr55* expression was measured by qPCR in sorted blood myeloid cells (Cd11b^{+}), T cells (CD3^{+}) and B cells (B220^{+}) to determine the B cell *Gpr55* depletion efficiency in *Gpr55*$^{-/-}$/*μMT*→*Ldlr*$^{-/-}$ mice ($n = 2$). Body weight ($n = 8–9$) (**c**) and total plasma cholesterol concentration (**d**) after 10 weeks of WD ($n = 8–9$; $^{*}P = 0.029$). **e**, Plaque area in aortic roots of bone marrow chimeric female mice after 10 weeks of WD ($n = 6–8$; $P = 0.049$). **f**, Representative Oil Red O-stained aortic root sections used for plaque quantification. **g**, Splenic B cell subsets assessed by flow cytometry ($n = 6–8$; exact *P* value is shown for each Ig subset in the graph). **h**, Average MFI of CD23 in the different B cell subsets ($n = 7–9$; exact *P* value is shown for each B cell subset in the graph). **i**, Plasma Ig titers at the end of the experiment ($n = 6–8$; exact *P* value is shown for each Ig subset in the graph). **j**, IgG antibodies against MDA-oxLDL in plasma after 10 weeks of WD ($n = 8–9$; $^{***}P = 0.0011$). Data were obtained in one bone marrow transplantation experiment, and each dot represents one biologically independent mouse sample (mean ± s.e.m.). Two-sided unpaired Student's *t*-test was used to determine the significant differences. KO, knockout.

the observed phenotype in global knockouts was not only due to B-cell-dependent effects but also modulated by T cell responses, such as Tfh interactions. Interestingly, we also observed changes in B cell CD23 expression levels but with different B cell subsets affected compared to global *Apoe*$^{-/-}$*Gpr55*$^{-/-}$ mice. In the chimeras with B-cell-specific deficiency, the CD23 expression level was lower in B1, B1b and B2 MZ cell subsets (Fig. 5h), suggesting a B-cell-intrinsic GPR55-dependent regulation of CD23 expression. Assessment of circulating antibody titers revealed slightly reduced plasma IgM titers, whereas IgGs were increased in B-cell-specific *Gpr55*-deficient mice (Fig. 5i), which is in line with the pro-atherogenic phenotype. In particular, we observed significantly increased plasma titers of MDA-LDL-specific IgGs, which points to an involvement of specific responses to OSE under hypercholesterolemic conditions (Fig. 5j).

Adoptive transfer of *Gpr55*$^{-/-}$ B cells fuels atherosclerosis

To substantiate the crucial importance of functional B cell GPR55 signaling in atherosclerosis, we performed an adoptive transfer experiment by injecting *Gpr55*$^{-/-}$ B cells into *Apoe*$^{-/-}$ mice. For this purpose, we treated *Apoe*$^{-/-}$ mice with a B-cell-depleting antibody cocktail and validated the depletion efficiency in blood and spleens in a pilot experiment (Fig. 6a,b). Next, we subjected *Apoe*$^{-/-}$ mice to the same depletion protocol before transferring WT or *Gpr55*$^{-/-}$ B cells. All experiments were performed with female recipients and cells from female donors. The adoptive transfer of *Gpr55*$^{-/-}$ B cells was sufficient to trigger an increase in plasma IgG levels and plaque size after 4 weeks of WD compared to the control group receiving WT B cells, without effects on body weight, plasma cholesterol and IgM levels (Fig. 6c–h). Moreover, the analysis of splenic B cell numbers revealed a decrease in almost all B cell subsets

https://doi.org/10.1038/s44161-022-00155-0

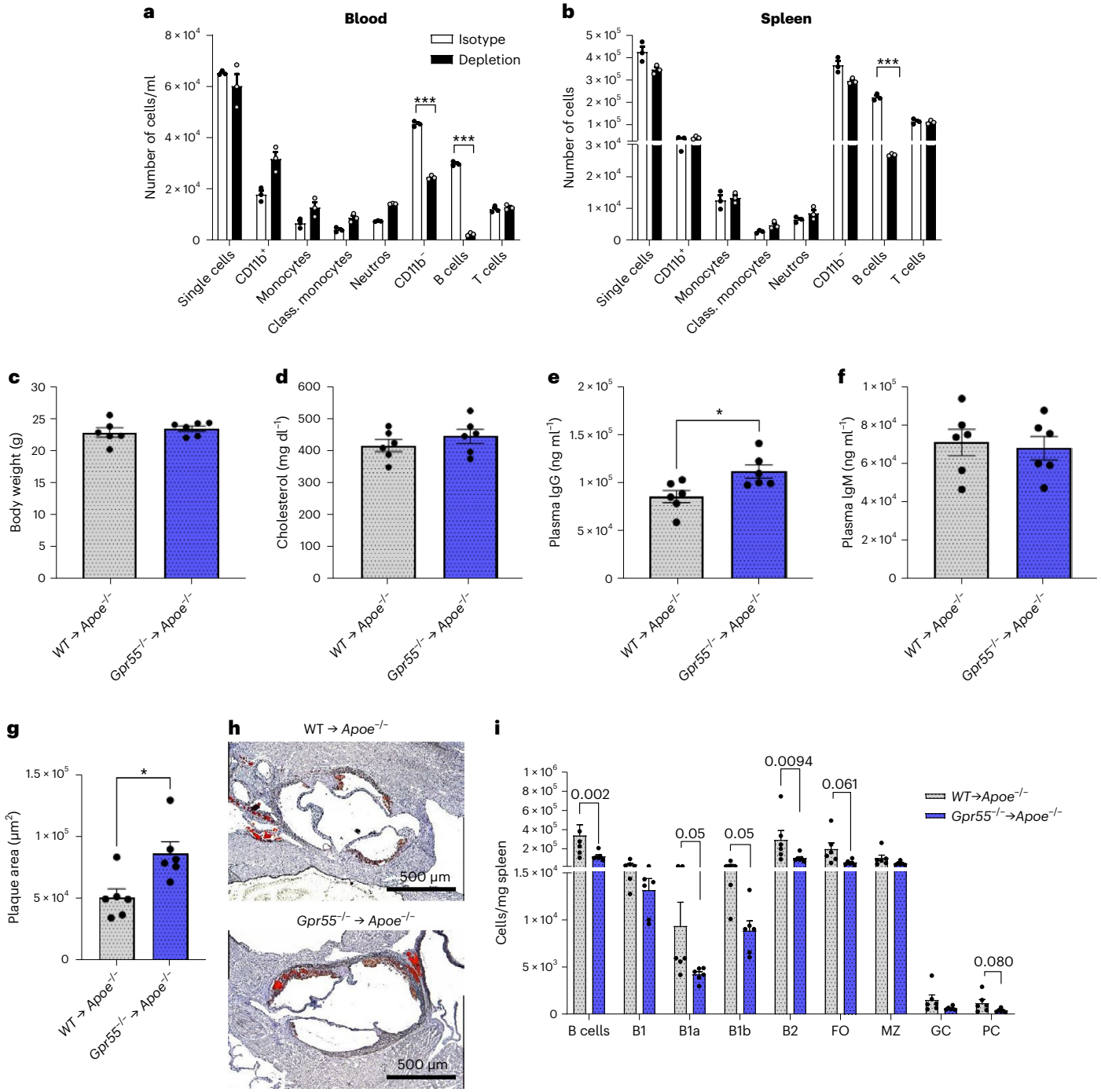

Fig. 6 | Impact of WT and *Gpr55*$^{-/-}$ adoptive B cell transfer into global *Apoe*$^{-/-}$ mice on atherosclerotic plaque formation and Ig titers. Circulating (**a**) and splenic (**b**) leukocyte counts in *Apoe*$^{-/-}$ mice treated with the B cell depletion cocktail or control animals treated with the respective isotype antibodies ($n = 3$ per group; ***$P < 0.0001$). Average body weight ($n = 6$) (**c**), total plasma cholesterol ($n = 6$) (**d**), IgG titers ($n = 6$; $P = 0.0125$) (**e**) and IgM titers (**f**) after 4 weeks of WD. Aortic root plaque size ($n = 6$; $P = 0.021$) (**g**) and representative Oil Red O-stained sections (**h**) of B-cell-depleted female *Apoe*$^{-/-}$ mice receiving WT or *Gpr55*$^{-/-}$ B cell adoptive transfer and subsequent WD feeding for 4 weeks. **i**, Splenic B cell subsets quantified by flow cytometry ($n = 6$). Data were obtained in one experiment (mean ± s.e.m.; $n = 6$ per group). Two-sided unpaired Student's *t*-test was used to determine the significant differences.

in *Gpr55*$^{-/-}$ compared to WT B cell recipients, including the B1a, total B2 and PC subsets (Fig. 6i), suggesting that *Gpr55*$^{-/-}$ B cell transfer was sufficient to confer an antibody-associated phenotype with disturbed splenic B cell differentiation.

Discussion

Our study provides previously unknown insights into the contribution of the lipid receptor GPR55 in atherosclerosis. Its role appears to be complex, ranging from metabolic to B-cell-specific effects. Mice with B-cell-specific *Gpr55* deficiency had reduced plasma cholesterol levels, which may suggest that *Gpr55* deficiency in B cells promotes lipid removal, for example, by increasing their surface expression of lipid-binding receptors[34], which is masked by the pro-steatotic effects in the global knockouts. Our liver metabolic data in the global *Apoe*$^{-/-}$*Gpr55*$^{-/-}$ mice are somewhat controversial to recent findings in hepatocytes, where a pro-steatotic function of GPR55 signaling was documented

by stimulation with the synthetic agonist O-1602, an effect that was reversed by the GPR55 antagonist CID16020046 (ref. [35]). These discrepancies might be explained, in part, by the fact that O-1602 also binds to GPR18 and different dietary conditions[36].

The finding that GPR55 is highly expressed by splenic PCs suggests a central role for GPR55 in this immune cell subset. However, our data support a more pleiotropic implication of GPR55 in B cells, affecting bone marrow differentiation, activation, GC formation and PC differentiation. GPR55 signaling exerts an atheroprotective effect in B cells, whereas the lack of GPR55 promotes an uncontrolled T and B cell interaction, leading to increased Tfh and circulating plasmablast counts, together with elevated plasma BAFF levels, thereby cumulating in an excessive IgG production. Many genes and pathways involved in B and T cell activation, cellular response to stress and intracellular signal transduction were differentially regulated in *Gpr55*-deficient B cells. Exploration of the Molecular Signatures Database (MSigDB) collection of immunologic signature gene sets highlighted the importance of GPR55 expression and signaling in antigen-specific and neutralizing antibody production and naive B cell activation and migration into the GC light and dark zones, where B cell clonal expansion, hypermutation and selection of high-affinity antibody-secreting PCs occurs[10]. Among the downregulated genes in *Apoe*$^{-/-}$*Gpr55*$^{-/-}$ B cells, *Fcer2a/CD23* and *Ptprc/LPAP* are positively correlated with *Gpr55* expression. Previous studies using CD23 knockout mouse models suggested that CD23 is not critical for B and T cell maturation but plays a regulatory function in the adaptive immune response[37]. Liu et al. demonstrated that CD23 negatively controls BCR signaling by inhibiting actin-mediated BCR clustering and B cell morphological changes[29]. Moreover, a link between CD23 expression and IgG antibody response has been proposed[38]. In particular, overexpression of CD23 resulted in significantly decreased IgG antibody responses. Hence, we may speculate that the decreased expression of CD23 in absence of GPR55 and, thus, lack of inhibitory signal for BCR signaling and IgG responses may contribute to the observed phenotype in our model. MZ and FO B cells are known to downregulate CD23 after undergoing isotype switch and memory B cell differentiation. In mice lacking CD23, antigen stimulation resulted in increased BCR clustering and F-actin at the cell surface[29], which phenocopies our observations in the *Apoe*$^{-/-}$*Gpr55*$^{-/-}$ mice. The different PC profile in mice with B-cell-specific *Gpr55* deficiency is likely related to the fact that GPR55 signaling in T cells is preserved. In addition, given that neutrophils also express relatively high levels of the receptor, we speculate that enhanced neutrophil inflammatory responses in absence of global GPR55 signaling lead to a more pronounced systemic inflammatory response and strong BCR activation. The plasma cell phenotype in B-cell-restricted *Gpr55* deficiency may be linked to antigen-independent constitutive BCR signaling, which promotes spontaneous PC differentiation. Less is known regarding *Ptprc*/LPAP in B cells. In vitro stimulation of *Ptprc* mutant B cells led to normal differentiation into plasmablasts, but the cells failed to downregulate B220 expression, albeit it did not affect their functionality[39].

The altered mitochondrial and actin cytoskeleton structure in *Gpr55*-deficient PCs is in agreement with an enhanced activation state. Activated B cells exposed to high levels of BAFF increased glucose uptake and mitochondrial mass, resulting in increased glycolysis and oxidative phosphorylation[40,41]. Although the mitochondrial dynamics in PCs have not been studied in detail, it is likely that IgG secretion in these cells is linked to increased metabolic rates and induces cellular stress responses[40,42–44]. The observed Ca^{2+} influx in response to LPI stimulation may play an important role in the regulation of cellular responses in PCs, including mitochondrial physiology and Ig production[45]. Lack of GPR55 signaling may reduce intracellular/ER Ca^{2+} stores, contributing to a defective BCR effector pathway activation. However, our in vitro experiments did not reveal changes in basal Ca^{2+} levels nor in response to the potent Ca^{2+} stimulus anti-IgM.

The role of LPI in B cell GPR55 signaling and atherogenesis remains incompletely understood. In vitro, LPI stimulated B cell maturation into PCs, which was inhibited when antagonizing GPR55. The effect was observed without addition of exogenous LPI, suggesting endogenously produced ligands in response to the inflammatory stimulation. In vivo, LPI treatment affected neither the plaque size nor the splenic B cell counts. Only a significant increase of plasma cholesterol levels was observed in LPI-treated mice compared to vehicle-treated mice. The reason for the lack of effects on atherosclerosis might be multifold. Given that LPI injection resulted in significantly elevated plasma cholesterol levels, which is in line with data reporting that 7 days of LPI injection induced liver steatosis[27], we may speculate that the pro-steatotic effects counterbalanced a possible atheroprotective phenotype. Moreover, LPI might not be stable enough to affect B cell differentiation in vivo. In addition, the local LPI release in splenic microdomains might be important to specifically act on plasmablasts in the red pulp or PCs in GCs. A better approach to address the in vivo relevance might be to block the enzymatic pathways involved in its degradation, which would require specific enzyme inhibitors to block LPI metabolic pathways. It is also possible that other endogenous GPR55 ligands (for example, palmitoylethanolamide) contribute to B cell GPR55 signaling[46]. Furthermore, LPI effects might be limited to atherogenesis, in line with the early peak of splenic *Gpr55* and *Ddhd1* expression as well as plasma LPI levels. This might be linked to the increase of circulating atherosclerosis-related antigens during onset of diet, thereby activating dendritic cells to release LPI, whereas this response is dampened in the more chronic disease state.

Another unresolved question remains the role of GPR55 in other immune subtypes. Our gene expression analysis of sorted splenic immune cell subsets indicates a strong GPR55 expression in T cells, which deserves further investigation in subsequent studies. The fact that GPR55 signaling in T cells is preserved may contribute to the observed differences in B cell subsets and antibody titers between the global and B-cell-specific deficiency models. Our study employing global and B-cell-specific in vivo approaches based on mixed bone marrow chimeras and adoptive B cell transfer at least confirms that GPR55 signaling in B cells crucially regulates atherosclerosis.

To conclude, our experimental in vivo and in vitro data, together with the confirmation of GPR55 expression and correlation with disease stage in human atherosclerosis, strongly support an implication of GPR55 in atherosclerosis. We uncovered a previously undescribed role for GPR55-LPI signaling in PC differentiation, at least in vitro. The transcriptomic signature and phenotype of *Gpr55*-deficient B cells supports that GPR55 provides a negative signal for BCR signaling with most prominent effects on CD23 regulation. However, the pleiotropic in vivo effects of *Gpr55* deficiency on B cell bone marrow differentiation, activation, GC formation and PC differentiation suggest a more general role of the receptor in the B cell lineage, which cannot be attributed to a single molecular mechanism. Orphan receptors such as GPR55, which are activated by bioactive lipid mediators, may represent an interesting therapeutic target to be further explored in the context of chronic inflammatory diseases, such as atherosclerosis and beyond.

Methods

Global *Gpr55*-deficiency mouse model of atherosclerosis

Gpr55$^{-/-}$ mice on C57BL/6J WT background were purchased from the European Mouse Mutant Archive (EM:02355), genotyped as previously reported[47] and back-crossed with *Apoe*$^{-/-}$ mice (strain 002052, Jackson Laboratory). Male and female *Apoe*$^{-/-}$ and *Apoe*$^{-/-}$*Gpr55*$^{-/-}$ mice aged 7–9 weeks were fed with WD (0.20% cholesterol, ssniff, TD88137) for 4 weeks, 10 weeks or 16 weeks. Female C57BL/6J and *Gpr55*$^{-/-}$ mice on C57BL/6J WT background were used at 6–8 weeks of age. At the endpoint, mice were anesthetized with ketamine/xylazine, and blood was obtained via cardiac puncture. Heart, aorta, spleen, femurs and livers were harvested after PBS perfusion. All animal experiments were

approved by the local ethics committee (District Government of Upper Bavaria; license nos.: 55.2-1-54-2532-111-13 and 55.2-2532.Vet_02-18-114) and conducted in accordance with institutional and national guidelines and following the ARRIVE guidelines. Animals were housed in individual ventilated cages in groups of 4–6 mice on a 12-hour light/dark cycle, air-conditioned (23 °C and 60% relative humidity), with ad libitum access to food pellets and tap water. Sample size for the experiments was selected for achieving an a priori 85% statistical power for biologically significant difference ($d = 0.8$).

B-cell-specific *Gpr55*-deficient bone marrow chimeras

Female *Ldlr*$^{-/-}$ mice (strain 002207, Jackson Laboratory), female *Gpr55*$^{-/-}$ mice on WT background and B-cell-deficient (*μMT*) female mice (strain 002288, Jackson Laboratory) aged 6–8 weeks at the start of experimental regimes were used. *Ldlr*$^{-/-}$ mice were irradiated with 8-Gy gamma radiation and reconstituted with 2×10^6 mixed bone marrow cells consisting of 50% *μMT* marrow and 50% *Gpr55*$^{-/-}$ or WT marrow, respectively. After irradiation, mice were recovered for 6 weeks and then subjected to WD feeding for 10 weeks. After the 6-week-recovery timepoint, tail vein blood was collected to assess the transplantation efficiency. At the endpoint, blood and organs were collected as described above.

Chronic LPI treatment

Age-matched and weight-matched littermate female *Apoe*$^{-/-}$ mice were randomly divided into two groups to receive daily i.p. injections of 0.1 mg kg^{-1} of LPI (L-α-lysophosphatidylinositol sodium salt from soybean; Sigma-Aldrich, 62966) or vehicle (0.05% Tween 80 and 0.1% DMSO in saline), respectively. Both groups were fed with WD for 4 weeks. At the endpoint, blood and organs were collected as described above.

Adoptive transfer of B cells

B cells were isolated from spleens of WT and *Gpr55*$^{-/-}$ female mice and enriched with a B cell isolation kit (Miltenyi Biotec MACS). The purity was 97 ± 1.2%. B cells were i.p. injected into B-cell-depleted female *Apoe*$^{-/-}$ mice (1×10^6 cells) treated 3 days before the adoptive B cell transfer with a cocktail of the following antibodies: B220 (clone RA3.3A1/6.1, ref: BE0067), CD19 (clone 1D3, ref: BE0150) and CD22 (clone Cy34.1, ref: BE0011) and, 48 hours later, anti-rat kappa (clone TIB216, ref: BE0122) (all antibodies from BioXCell; 150 μg i.p. per antibody). To test the B cell depletion efficiency, some mice were treated with a depletion antibody cocktail or isotype (IgG1, ref: BE0083, BioXCell) and euthanized 72 hours after the first injection to measure leukocyte counts in the blood and spleen by flow cytometry. At the endpoint, blood and organs were collected as described above.

Human material

The permission to collect human carotid atherosclerotic biospecimens for the Munich Vascular Biobank was approved by the local hospital ethics committee (Ethikkommission der Fakultät für Medizin der Technischen Universität München). All patients provided their written informed consent. Human carotid artery plaques were harvested during carotid artery endarterectomy surgery, transported to the laboratory and snap-frozen. Carotid tissue with an unstable/ruptured or stable plaque phenotype, depending on symptoms of plaque instability and the size of the fibrous cap (cutoff of 200 μm)[48,49] was cut in ~50-mg pieces on dry ice. Patient characteristics are summarized in Extended Data Table 1. The tissue homogenization was performed in 700-μl QIAzol lysis reagent, and total RNA was isolated using the miRNeasy Mini Kit (Qiagen) according to the manufacturer's instruction. RNA concentration and purity were assessed using NanoDrop. RIN number was assessed using the RNA Screen Tape (Agilent) in the Agilent TapeStation 4200. Next, first-strand cDNA synthesis was performed using the High-Capacity-RNA-to-cDNA Kit (Applied Biosystems), following the manufacturer's instructions. Quantitative real-time PCR was performed in 96-well plates with a QuantStudio3 Cycler (Applied Biosystems) using TaqMan Gene Expression Assays (Thermo Fisher Scientific) for detection of the following expressed genes: *RPLPO* (Hs99999902_m1) and *GPR55* (Hs00271662_s1).

Cholesterol and triglyceride measurement

Liver tissue (50–70 mg) was homogenized in 500 μl of 0.1 % NP-40 in PBS using a bead mill Tissue Lyser (Qiagen) and centrifuged for 2 minutes at 3,000*g* to remove the insoluble material. Total plasma cholesterol and triglyceride concentrations were quantified in murine plasma and liver homogenates using colorimetric assays (CHOD-PAP and TAG-PAP Roche) according to the manufacturer's protocol.

Lipoprotein profile analysis

Plasma samples were subjected to fast-performance liquid chromatography (gel filtration on a Superose 6 column, GE Healthcare). Different lipoprotein fractions (VLDL, LDL and high-density lipoprotein (HDL)) were separated and evaluated based on flow-through time.

LPI analysis by liquid chromatography–tandem mass spectrometry

Plasma samples were allowed to thaw on ice water, and 50-μl aliquots were transferred to 1.5-ml centrifugation tubes. After adding 300 μl of ice-cold ethyl acetate/hexane (9:1, v/v) containing the deuterated LPI as internal standards, tubes were vortexed and centrifuged for 15 minutes at 20,000*g* at 4 °C. The upper organic phase was removed, evaporated to dryness under a gentle stream of nitrogen at 37 °C and reconstituted in 50 μl of acetonitrile/water (1:1, v/v). Plasma concentrations of LPI were determined by liquid chromatography multiple reaction monitoring and normalized to the total volume of supernatant[50]. Only LPI 20:4 was targeted and quantified, whereas other LPI species with other fatty acyl composition, such as LPI 16:0 and LPI 18:0, were excluded based on retention time and transition of precursor *m*/*z* to fragment *m*/*z*. Isoforms of LPI 20:4, such as sn1/sn2 *cis*/*trans* or position of double bond within the LPI 20:4 composition, were not detected/included.

Histological studies

Mouse hearts and livers were isolated after perfusion with PBS and frozen in Tissue-Tek (Sakura Finetek). Aortic roots were cut in 4-μm-thick and liver sections in 5-μm-thick serial cryosections. The sections were stained with Oil Red O for total plaque and lipid analysis, and aortic roots were also stained with Masson's trichrome for collagen in accordance with the guidelines for experimental atherosclerosis studies by the AHA[51]. Lesion size was analyzed in a blinded manner and quantified in eight sections per heart, separated by 40 μm from each other, to cover the entire aortic root. For conventional immunofluorescence, aortic root sections were fixed for 5 minutes with 4% formalin and blocked for 1 hour at room temperature with blocking buffer (PBS with 1% BSA). Then, the slides were incubated with Mac2 primary antibody overnight at 4 °C for macrophage staining, followed by anti-rat-AF488 for 2 hours at room temperature and nuclear staining (Hoechst 33342) for 5 minutes. Images were acquired using a Leica DM6000B fluorescence microscope equipped with a digital camera (DFC365, Leica). The Leica Application Suite LAS V4.3 software or ImageJ software were used for the lipid, plaque and macrophage quantification. Splenic cryosections of 10-μm thickness were fixed for 5 minutes with 4% formalin and blocked for 1 hour at room temperature and then stained with directly conjugated antibodies overnight at 4 °C. PNA-FITC (1:100) was used for GC B cells; IgM-AF647 (1:250) was used for MZ B cells and memory B cells; CD23-AF594 (1:100) was used for FO B cells; and Hoechst 33342 was used for the nuclei staining. Digital images were acquired using a three-dimensional (3D) confocal laser scanning microscope (CLSM; Leica SP8 3X) equipped with a ×100, NA 1.40 oil immersion objective (Leica).

In situ hybridization

In situ hybridization was performed with a murine *Gpr55* probe (VB6-3216575, Affymetrix). Splenic sections were cut and collected in RNAse-free slides, pre-fixed in 4% paraformaldehyde for 5 minutes at room temperature and washed three times with PBS for 5 minutes. The tissue sections were then treated with pre-warmed 10 µg ml^{-1} of Proteinase K (diluted in PBS) for 5 minutes at room temperature, followed by post-fixing with 100% ethanol for 1 minute. After washing with PBS, the sections were transferred to an RNAse-free chamber. The ViewRNA Cell Plus Assay Kit (Invitrogen) was used for target probe hybridization by incubating the sections at 40 °C for 2 hours. The hybridization probe was mixed with probe set diluent to a final concentration of 5 µg ml^{-1}. After the hybridization step, the sections were washed, and a signal amplification was performed by incubating with the pre-amplifier mix for 30 minutes at 40 °C, washing and incubating with the amplifier mix for 1 hour at 40 °C. After washing, the sections were incubated for 1 hour at 40 °C with the working label probe mix. After the in situ hybridization for the *Gpr55* probe, the sections were washed, incubated with blocking buffer at room temperature for 1 hour and stained with PNA-FITC, IgM-AF647 and CD23-AF594 antibodies as described above.

Flow cytometry

Splenic single-cell suspensions were obtained by mashing the spleens through a 70-µm cell strainer. Femurs were centrifuged at 10,000*g* for 1 minute after exposure of the distal metaphysis to collect the bone marrow cells. Splenic, bone marrow and blood erythrocytes were lysed with ammonium-chloride-potassium (ACK; NH_4Cl (8,024 mg L^{-1}), $KHCO_3$ (1,001 mg L^{-1}) and EDTA.$Na_2{\cdot}2H_2O$ (3.722 mg L^{-1})) buffer for 10 minutes at room temperature. For staining of leukocytes infiltrated into the aorta, the vessels were excised from the aortic arch to iliac bifurcation and digested with collagenase IV and DNase I at 37 °C at 750 r.p.m. for 40 minutes[52] and filtered through a 30-µm cell strainer. Blood, splenic, bone marrow and aortic single cells were blocked for 5 minutes with Fc-CD16/CD32 antibody and then stained for 30 minutes in the dark at 4 °C with antibodies (Supplementary Table 1) to identify cell subsets. After gating for living singlets and CD45$^+$, the CD11b$^+$ myeloid subsets were further gated as follows: CD115$^+$Ly6G$^-$ (monocytes), F4/80$^+$ (macrophages) and CD115$^-$Ly6G$^+$ (neutrophils). The CD11b$^-$ lymphoid population was divided into CD3$^+$ (T cells) and CD19$^+$ (B cells). B cell subsets were further identified as B220^{low}CD23$^-$CD5$^+$ (B1a), B220^{low}CD23$^-$CD5$^-$ (B1b), B220^{high}CD23$^-$IgM$^+$ (MZ), B220^{high}CD23$^-$IgM^{int}IgD$^+$ (FO) and B220^{high}CD23$^+$IgM^{int}PNA$^+$GL7$^+$ (GC) (Extended Data Fig. 4). PCs were gated as CD19$^-$CD138$^+$CD23$^-$IgM$^-$IgD$^-$, and splenic Tfh cells were gated as CD3$^+$CD19$^-$CXCR5$^+$PD1$^+$. The circulating plasmablasts were identified as CD19$^+$CD38$^+$CD138$^+$, and long-lived bone marrow PCs were identified as CD19$^-$CD138$^+$. Lymphoid and B cell progenitor populations were gated as follows: lin$^-$(CD3$^-$CD11b$^-$B220$^-$Gr1$^-$Ter119$^-$) and CD127$^+$(CLP), lin$^-$B220$^+$CD19$^-$CD43$^+$ (pre-proB), lin$^-$B220$^+$CD19$^+$CD43$^+$ (proB), lin$^-$CD19$^+$CD43$^-$CD24$^+$CD127$^+$ (pre-B), lin$^-$CD19$^+$IgM$^+$ (immature B cells) and lin$^-$CD19$^+$CD43$^-$CD24$^+$CD127$^-$IgD$^+$ (activated B cells).

For mitochondrial staining in splenic and bone marrow B cells, the cells were incubated with pre-warmed (37 °C) staining solution containing MitoTracker (Thermo Fisher Scientific) at a concentration of 50 nM for 30 minutes. After removing the mitochondrial staining solution by centrifugation, the cells were stained with specific antibodies to identify the different B cell subpopulations. Flow cytometry data were acquired on a BD FACSCanto II flow cytometer (BD Biosciences) or Fortessa LSR (BD Biosciences) and analyzed with FlowJo version 10.2 software (Tree Star).

Flow cytometric sorting of splenic B cells

Single-cell suspensions obtained from *Apoe*$^{-/-}$ and *Apoe*$^{-/-}$*Gpr55*$^{-/-}$ spleens were sorted using a BD FACSAria III Cell Sorter (BD Biosciences) as CD19$^+$ total B cells or B220^{high}CD23$^+$IgM^{int}PNA$^+$GL7$^+$ GC cells. Circulating plasmablasts were gated as CD19$^+$CD38$^+$CD138$^+$, and bone marrow long-lived PCs were identified as CD19$^-$CD138$^+$. The sorted cells were deep-frozen in 2× TCL buffer (Qiagen) plus 1% beta-mercaptoethanol.

RNA sequencing and analysis

Sorted cells were used to perform bulk RNA sequencing using the prime-seq protocol that can be found on protocols.io (https://doi.org/10.17504/protocols.io.s9veh66)[28]. In brief, 10,000 sorted cells were lysed in 100 µl of RLT$^+$ and 1% beta-mercaptoethanol, and 50 µl of lysate was used for RNA sequencing. In case that fewer than 10,000 cells were obtained, all sorted cells were used. The samples were Proteinase K and DNase I digested, and then cDNA synthesis was performed using uniquely barcoded oligodT primers. Samples destined for the same library were pooled, and pre-amplification was then performed using 11–14 cycles, depending on the initial input per library. The cDNA was quantified using the PicoGreen dsDNA Assay Kit (Thermo Fisher Scientific, P11496) and qualified using the Bioanalyzer HS DNA chip (Agilent, 5067–4626). Libraries were then constructed with the NEB Next Ultra II FS Kit (E6177S, New England Biolabs) using the prime-seq specifications. The libraries were quantified and qualified using the HS DNA chip on the Bioanalyzer and sequenced on an Illumina HiSeq 1500 at an average depth of 12.7 million reads per sample. The reads were demultiplexed using deML and then filtered, mapped to the mouse genome (mm10, GRCm38) and counted using zUMIs (version 2.5.5) with STAR[53]. Differential gene expression analysis was performed using DESeq2, and then the characterization of the molecular functions or pathways in which DEGs are involved was performed using GSEA. In addition, GSEA software was used to find immunological gene set annotations by using the ImmuneSigDB subset (C7) MSigDB[54–57]. Other resources used were GO, Bioconductor, Gorilla and DAVID.

Quantitative real-time PCR

Aortas, sorted leukocytes and splenic B cell subsets were homogenized and lysed for extraction of total RNA (peqGOLD TriFast and Total RNA Kit, Peqlab). After reverse transcription (PrimeScript RT Reagent Kit, Clontech), real-time PCR was performed with the 7900HT Sequence Detection System (Applied Biosystems) using the KAPA PROBE FAST Universal qPCR Kit (Peqlab). Primers and probes were purchased from Life Technologies. Target gene expression was normalized to *Hprt* (hypoxanthine-guanine phosphoribosyltransferase) and presented as relative transcript level ($2^{-\Delta\Delta C_T}$). For comparison of *Gpr55* expression, *Gapdh* (glyceraldehyde-3-phosphate dehydrogenase) was used as additional housekeeping control for normalization (Supplementary Table 2).

ddPCR

For performing the ddPCR, we prepared the reaction mixture by combining a 2× ddPCR Mastermix (Bio-Rad), 20× primer and probes (final concentrations of 900 nM and 250 nM, respectively; Integrated DNA Technologies) and template in a final volume of 20 µl (Supplementary Table 3). Then, each ddPCR reaction mixture was loaded into the sample well of an eight-channel disposable droplet generator cartridge (Bio-Rad). A volume of 60 µl of droplet generation oil (Bio-Rad) was loaded into the oil well for each channel. The cartridge was placed into the droplet generator (Bio-Rad), and the droplets were collected and transferred to a 96-well PCR plate. The plate was heat-sealed with a foil seal, placed on the thermal cycler and amplified to the endpoint (40 cycles). After PCR, the 96-well PCR plate was loaded on the droplet reader (Bio-Rad). Analysis of the ddPCR data was performed with QuantaSoft analysis software (Bio-Rad).

Ig measurement in plasma

To measure Ig isotypes and subclasses in plasma, the Antibody Isotyping 7-Plex Mouse ProcartaPlex Panel was performed with a MAGPIX luminex reader (Thermo Fisher Scientific). For total IgG and IgM

quantification, single ELISA kits were used (Thermo Fisher Scientific). Anti-MDA-specific IgGs were measured by coating MaxiSorp plates (NuncTM) with purified, mouse-derived delipidated apolipoprotein MDA for 1 hour at 37 °C. After being washed, all wells were blocked for 1 hour with 2% BSA in PBS at 37 °C. Mouse samples were also added to a non-coated well to assess individual non-specific binding. After washing, 50 µl per well of the alkaline phosphatase-conjugated anti-mouse IgG was added (Sigma-Aldrich) diluted at 1:1,000 in a PBS/BSA 2% solution and incubated for 1 hour at 37 °C. After washing, phosphatase substrate p-nitrophanylphosphate disodium (Sigma-Aldrich) dissolved in a diethanolamine buffer (pH 9.8) was added and incubated for 30 minutes at 37 °C. Optical density (OD) was determined at 405 nm (FilterMax 3, Molecular Devices), and each sample was tested in duplicate. Corresponding non-specific binding was subtracted from mean OD for each sample.

In vitro PC differentiation

Splenic B cells were isolated from *Apoe*$^{-/-}$ and *Apoe*$^{-/-}$*Gpr55*$^{-/-}$ mice by meshing the spleen and subsequent enrichment for CD19^{+} cells using a Miltenyi kit. For PC in vitro differentiation, the isolated B cells were seeded in 24-well plates and treated with a cocktail of LPS (0.5 ng ml^{-1}), IFN-α (2 ng ml^{-1}), IL2 (5 ng ml^{-1}), IL4 (5 ng ml^{-1}) and IL5 (2 ng ml^{-1}) for 7 days, adding fresh medium with the stimulation cocktail every second day, based on an optimized protocol according to previous publications[58,59]. In some conditions, the stimulation cocktail was combined with LPI (Sigma-Aldrich, 62966) or CID16020046. After 7 days, cells were collected and used for flow cytometric analysis of the total number of PCs, gated as viable single CD45^{+}CD11b^{-}CD19^{+}CD138^{+} cells. For mitochondrial staining, the cells were incubated with pre-warmed (37° C) staining solution containing MitoTracker (Thermo Fisher Scientific) at a concentration of 50 nM for 30 minutes. After removing the mitochondrial staining solution by centrifugation, the cells were stained with specific antibodies to identify the PCs. Flow cytometry data were acquired on a BD FACSCanto II flow cytometer (BD Biosciences) and analyzed with FlowJo version 10.2 software (Tree Star).

Confocal/STED imaging of splenic PCs

Splenic B cells were isolated from *Apoe*$^{-/-}$ and *Apoe*$^{-/-}$*Gpr55*$^{-/-}$ mice, seeded into glass-bottom chamber eight-well slides (Ibidi) and differentiated into PCs as described above. We stained the mitochondria following the above-described protocol, and then the slides were subsequently stained with F-actin for 30 minutes at room temperature, followed by incubation for 5 minutes with Hoechst 33342 (Thermo Fisher Scientific) and embedded with ProLong Diamond Antifade Mountant (Thermo Fisher Scientific). Digital images were acquired using a 3D CLSM combined with STED (Leica SP8 3X) equipped with a ×100, NA 1.40 oil immersion objective (Leica). Optical zoom was used where applicable. For fluorescence excitation, a UV laser (405 nm) was used for excitation of Hoechst and a tunable white light laser for selective excitation of other fluorochromes (Alexa Fluor 488, Alexa Fluor 594 and Alexa Fluor 647). Depletion was performed at 592 nm and 775 nm for Alexa Fluor 488 and Alexa Fluor 594, respectively. Images were collected in a sequential scanning mode using hybrid diode detectors to maximize the signal collection and reduce the background noise and overlap between the channels. All data were acquired in three dimensions, and voxel size was determined according to Nyquist sampling criterion. Image reconstructions were performed using the LAS X software package version 3.0.2 (Leica), and deconvolution was applied in combination with the Huygens Professional software package version 19.10 (Scientific Volume) using the unsupervised CMLE (for CLSM) algorithm. Visualization of 3D images is provided as a video showing the merged fluorescent channels from different visual perspectives (Supplementary Video). To this end, 3D rendering was performed using LAS X 3D software, and visual perspective was automatically selected by the software to provide the best visualization.

Ca^{2+} assay and CD23 stimulation

Ca^{2+} responses and CD23 surface expression were measured in human blood of healthy donors and murine blood isolated from female baseline (normal diet fed) WT mice, baseline or 10 weeks of WD-fed *Apoe*$^{-/-}$ mice and baseline *Apoe*$^{-/-}$*Gpr55*$^{-/-}$ mice. In brief, the cells were stained with an antibody cocktail to identify B cells, washed and then incubated with FLIPR Calcium 5 Assay Kit (Molecular Devices) for 1 hour at 37 °C. Human B cells were identified by staining with CD45-AF700 (Biolegend, 368513), CD19-PE-Dazzle (Biolegend, 115554) and CD20- APC (Biolegend, 302309). Murine B cells were gated as CD45^{+}CD11b^{-}CD19^{+}. After stimulation with soybean LPI (Sigma-Aldrich, 62966) or pure 20:4 LPI (Sigma-Aldrich, 850105P) for 30 seconds, the samples were immediately analyzed by flow cytometry to determine the mean fluorescence intensity (MFI) of intracellular Ca^{2+}. The CD23 surface expression was measured after 10–60 minutes of LPI stimulation.

Statistical analysis

Statistical analyses were performed using GraphPad Prism version 9.1.1 software (GraphPad Software). To test for Gaussian distribution, D'Agostino–Pearson omnibus or Shapiro–Wilk normality test was applied. Outliers were determined by Grubbs' test (alpha = 0.05). After testing homogeneity of variances via *F*-test, Student's *t*-test was used for normally distributed data with equal variances. For heteroscedastic data, Welch correction was applied. Mann–Whitney *U*-test was performed if normality test failed. Comparisons among more than two groups were made by one-way or two-way ANOVA with Tukey post hoc test or Kruskal–Wallis test with Dunn post hoc test, as indicated in each figure legend. Bivariate correlations involving *Gpr55* expression, plaque area or plasma IgG were analyzed by Spearman's rank correlation test, to avoid assumptions on data distribution. All data are shown as mean ± s.e.m. A two-tailed $P < 0.05$ was considered statistically significant.

Reporting summary

Further information on research design is available in the Nature Research Reporting Summary linked to this article.

Data availability

The RNA sequencing data are accessible under Gene Expression Omnibus accession number GSE211594.

References

1. Libby, P. et al. Atherosclerosis. *Nat. Rev. Dis. Primers* **5**, 56 (2019).
2. Libby, P. The changing landscape of atherosclerosis. *Nature* **592**, 524–533 (2021).
3. Galkina, E. & Ley, K. Immune and inflammatory mechanisms of atherosclerosis (*). *Annu. Rev. Immunol.* **27**, 165–197 (2009).
4. Hill, C. A., Fernandez, D. M. & Giannarelli, C. Single cell analyses to understand the immune continuum in atherosclerosis. *Atherosclerosis* **330**, 85–94 (2021).
5. Srikakulapu, P. & McNamara, C. A. B cells and atherosclerosis. *Am. J. Physiol. Heart Circ. Physiol.* **312**, H1060–H1067 (2017).
6. Kyaw, T., Tipping, P., Bobik, A. & Toh, B.-H. Opposing roles of B lymphocyte subsets in atherosclerosis. *Autoimmunity* **50**, 52–56 (2017).
7. Aziz, M., Holodick, N. E., Rothstein, T. L. & Wang, P. The role of B-1 cells in inflammation. *Immunol. Res.* **63**, 153–166 (2015).
8. Tsiantoulas, D., Diehl, C. J., Witztum, J. L. & Binder, C. J. B cells and humoral immunity in atherosclerosis. *Circ. Res.* **114**, 1743–1756 (2014).
9. Stebegg, M. et al. Regulation of the germinal center response. *Front. Immunol.* **9**, 2469 (2018).
10. Victora, G. D. & Nussenzweig, M. C. Germinal centers. *Annu. Rev. Immunol.* **40**, 413–442 (2022).
11. Sage, A. P., Tsiantoulas, D., Binder, C. J. & Mallat, Z. The role of B cells in atherosclerosis. *Nat. Rev. Cardiol.* **16**, 180–196 (2019).

12. Lorenzo, C. et al. ALDH4A1 is an atherosclerosis auto-antigen targeted by protective antibodies. *Nature* **589**, 287–292 (2021).
13. Nus, M. et al. Marginal zone B cells control the response of follicular helper T cells to a high-cholesterol diet. *Nat. Med.* **23**, 601–610 (2017).
14. Immunological Genome Project. ImmGen at 15. *Nat. Immunol.* **21**, 700–703 (2020).
15. Guillamat-Prats, R., Rami, M., Herzig, S. & Steffens, S. Endocannabinoid signalling in atherosclerosis and related metabolic complications. *Thromb. Haemost.* **119**, 567–575 (2019).
16. Puhl, S.-L. Cannabinoid-sensitive receptors in cardiac physiology and ischaemia. *Biochim. Biophys. Acta Mol. Cell. Res.* **1867**, 118462 (2020).
17. Drzazga, A., Sowińska, A. & Koziołkiewicz, M. Lysophosphatidylcholine and lysophosphatidylinosiol—novel promissing signaling molecules and their possible therapeutic activity. *Acta Pol. Pharm.* **71**, 887–899 (2014).
18. Sumida, H. et al. GPR55 regulates intraepithelial lymphocyte migration dynamics and susceptibility to intestinal damage. *Sci. Immunol.* **2**, eaao1135 (2017).
19. Lanuti, M., Talamonti, E., Maccarrone, M. & Chiurchiù, V. Activation of GPR55 receptors exacerbates oxLDL-induced lipid accumulation and inflammatory responses, while reducing cholesterol efflux from human macrophages. *PLoS ONE* **10**, e0126839 (2015).
20. Wang, Y., Pan, W., Wang, Y. & Yin, Y. The GPR55 antagonist CID16020046 protects against ox-LDL-induced inflammation in human aortic endothelial cells (HAECs). *Arch. Biochem. Biophys.* **681**, 108254 (2020).
21. Montecucco, F. et al. Treatment with the GPR55 antagonist CID16020046 increases neutrophil activation in mouse atherogenesis. *Thromb. Haemost.* **116**, 987–997 (2016).
22. Veillard, N. R., Steffens, S., Burger, F., Pelli, G. & Mach, F. Differential expression patterns of proinflammatory and antiinflammatory mediators during atherogenesis in mice. *Arterioscler. Thromb. Vasc. Biol.* **24**, 2339–2344 (2004).
23. Stary, H. C. et al. A definition of advanced types of atherosclerotic lesions and a histological classification of atherosclerosis. A report from the Committee on Vascular Lesions of the Council on Arteriosclerosis, American Heart Association. *Circulation* **92**, 1355–1374 (1995).
24. Redgrave, J. N., Gallagher, P., Lovett, J. K. & Rothwell, P. M. Critical cap thickness and rupture in symptomatic carotid plaques: the oxford plaque study. *Stroke* **39**, 1722–1729 (2008).
25. Horikawa, K. et al. Enhancement and suppression of signaling by the conserved tail of IgG memory-type B cell antigen receptors. *J. Exp. Med.* **204**, 759–769 (2007).
26. Haerzschel, A. et al. BCR and chemokine responses upon anti-IgM and anti-IgD stimulation in chronic lymphocytic leukaemia. *Ann. Hematol.* **95**, 1979–1988 (2016).
27. Fondevila, M. F. et al. The L-α-lysophosphatidylinositol/G protein-coupled receptor 55 system induces the development of nonalcoholic steatosis and steatohepatitis. *Hepatology* **73**, 606–624 (2021).
28. Janjic, A. et al. Prime-seq, efficient and powerful bulk RNA-sequencing. *Genome Biol.* **23**, 88 (2022).
29. Liu, C. et al. CD23 can negatively regulate B-cell receptor signaling. *Sci. Rep.* **6**, 25629 (2016).
30. Kleiman, E. et al. Distinct transcriptomic features are associated with transitional and mature B-cell populations in the mouse spleen. *Front. Immunol.* **6**, 30 (2015).
31. Chevrier, S. et al. The BTB-ZF transcription factor Zbtb20 is driven by Irf4 to promote plasma cell differentiation and longevity. *J. Exp. Med.* **211**, 827–840 (2014).
32. Recaldin, T. & Fear, D. J. Transcription factors regulating B cell fate in the germinal centre. *Clin. Exp. Immunol.* **183**, 65–75 (2016).
33. Bhat, T. A. et al. Endoplasmic reticulum-mediated unfolded protein response and mitochondrial apoptosis in cancer. *Biochim. Biophys. Acta Rev. Cancer* **1867**, 58–66 (2017).
34. Echeverri Tirado, L. C. & Yassin, L. M. B cells interactions in lipid immune responses: implications in atherosclerotic disease. *Lipids Health Dis.* **16**, 30 (2017).
35. Kang, S., Lee, A.-Y., Park, S.-Y., Liu, K.-H. & Im, D.-S. O-1602 promotes hepatic steatosis through GPR55 and PI3 kinase/Akt/SREBP-1c signaling in mice. *Int. J. Mol. Sci.* **22**, 3091 (2021).
36. Console-Bram, L., Brailoiu, E., Brailoiu, G. C., Sharir, H. & Abood, M. E. Activation of GPR18 by cannabinoid compounds: a tale of biased agonism. *Br. J. Pharmacol.* **171**, 3908–3917 (2014).
37. Stief, A. et al. Mice deficient in CD23 reveal its modulatory role in IgE production but no role in T and B cell development. *J. Immunol.* **152**, 3378–3390 (1994).
38. Payet, M. E., Woodward, E. C. & Conrad, D. H. Humoral response suppression observed with CD23 transgenics. *J. Immunol.* **163**, 217–223 (1999).
39. Yabas, M., Yazicioglu, Y. F., Hoyne, G. F., Goodnow, C. C. & Enders, A. Loss of hnRNPLL-dependent splicing of *Ptprc* has no impact on B-cell development, activation and terminal differentiation into antibody-secreting cells. *Immunol. Cell Biol.* **99**, 532–541 (2021).
40. Xie, J.-H., Li, Y.-Y. & Jin, J. The essential functions of mitochondrial dynamics in immune cells. *Cell. Mol. Immunol.* **17**, 712–721 (2020).
41. Caro-Maldonado, A. et al. Metabolic reprogramming is required for antibody production that is suppressed in anergic but exaggerated in chronically BAFF-exposed B cells. *J. Immunol.* **192**, 3626–3636 (2014).
42. Breda, C. N. et al. Mitochondria as central hub of the immune system. *Redox Biol.* **26**, 101255 (2019).
43. Jang, K.-J. et al. Mitochondrial function provides instructive signals for activation-induced B-cell fates. *Nat. Commun.* **6**, 6750 (2015).
44. Urbanczyk, S. et al. Mitochondrial respiration in B lymphocytes is essential for humoral immunity by controlling the flux of the TCA cycle. *Cell Rep.* **39**, 110912 (2022).
45. Scharenberg, A. M., Humphries, L. A. & Rawlings, D. J. Calcium signalling and cell-fate choice in B cells. *Nat. Rev. Immunol.* **7**, 778–789 (2007).
46. Rinne, P. et al. Palmitoylethanolamide promotes a proresolving macrophage phenotype and attenuates atherosclerotic plaque formation. *Arterioscler. Thromb. Vasc. Biol.* **38**, 2562–2575 (2018).
47. Puhl, S.-L. et al. Haematopoietic and cardiac GPR55 synchronize post-myocardial infarction remodelling. *Sci. Rep.* **11**, 14385 (2021).
48. Jin, H. et al. Local delivery of miR-21 stabilizes fibrous caps in vulnerable atherosclerotic lesions. *Mol. Ther.* **26**, 1040–1055 (2018).
49. Eken, S. M. et al. MicroRNA-210 enhances fibrous cap stability in advanced atherosclerotic lesions. *Circ. Res.* **120**, 633–644 (2017).
50. Bindila, L. & Lutz, B. Extraction and simultaneous quantification of endocannabinoids and endocannabinoid-like lipids in biological tissues. *Methods Mol. Biol.* **1412**, 9–18 (2016).
51. Daugherty, A. et al. Recommendation on design, execution, and reporting of animal atherosclerosis studies: a scientific statement from the American Heart Association. *Arterioscler. Thromb. Vasc. Biol.* **37**, e131–e157 (2017).
52. Sager, H. B. et al. RNAi targeting multiple cell adhesion molecules reduces immune cell recruitment and vascular inflammation after myocardial infarction. *Sci. Transl. Med.* **8**, 342ra80 (2016).
53. Dobin, A. et al. STAR: ultrafast universal RNA-seq aligner. *Bioinformatics* **29**, 15–21 (2013).

54. Subramanian, A. et al. Gene set enrichment analysis: a knowledge-based approach for interpreting genome-wide expression profiles. *Proc. Natl Acad. Sci. USA* **102**, 15545–15550 (2005).
55. Liberzon, A. et al. The Molecular Signatures Database (MSigDB) hallmark gene set collection. *Cell Syst.* **1**, 417–425 (2015).
56. Liberzon, A. et al. Molecular Signatures Database (MSigDB) 3.0. *Bioinformatics* **27**, 1739–1740 (2011).
57. Godec, J. et al. Compendium of immune signatures identifies conserved and species-specific biology in response to inflammation. *Immunity* **44**, 194–206 (2016).
58. Maïga, R. I., Bonnaure, G., Rochette, J. T. & Néron, S. Human $CD38^{hi}CD138^{+}$ plasma cells can be generated in vitro from CD40-activated switched-memory B lymphocytes. *J. Immunol. Res.* **2014**, 635108 (2014).
59. Jourdan, M. et al. An in vitro model of differentiation of memory B cells into plasmablasts and plasma cells including detailed phenotypic and molecular characterization. *Blood* **114**, 5173–5181 (2009).

Acknowledgements

We are deeply grateful to M. Aslani for advice on transcriptomic data visual presentation, and we thank D. Wagner, Y. Jansen, R. Carrasco-Leon, B. Dufner and S. Wolkerstorfer for excellent technical support. The authors received funds from the Deutsche Forschungsgemeinschaft (DFG) (STE1053/6-1 and STE1053/8-1 to S. Steffens and SFB1123 to S. Steffens, C.W. and L.M.), the German Ministry of Research and Education (DZHK FKZ 81Z0600205 to S. Steffens), the European Research Council (ERC-AdG 69251 to C.W.) and the LMU Medical Faculty FöFoLe program (1061 to R.G.P.). I.H. is supported by the DFG (HI1573/2 and CRC1425 422681845).

Author contributions

R.G.-P., D.H. and M.R. designed and performed experiments and analyzed and interpreted data, supervised by S. Steffens. A.D. contributed to the in vivo revision experiments and tested GPR55 antibody specificity by western blotting. C.H. and I.H. designed the B cell bone marrow transplant experiment, and I.H. gave critical input for the entire study design. D.S. provided expertise for confocal/STED imaging and statistical analysis. P.R. contributed to the histological analysis. L.B. performed lipidomic measurements. S.P. and N.V. determined MDA-oxLDL antibodies in plasma. M.H. conducted cell sorting. A.J. and W.E. performed the bulk RNA sequencing and the cleanup of the obtained data. S. Schmid and L.M. determined *GPR55* expression in human plaques. A.F. guided the Ca^{2+} assays and provided critical input to the study. C.W. provided scientific infrastructure and advice for the study design. R.G.-P. and S. Steffens designed the study and wrote the manuscript. All authors contributed to the final manuscript editing and approved the submitted version.

Competing interests

The authors declare no competing interests.

Additional information

Extended data is available for this paper at https://doi.org/10.1038/s44161-022-00155-0.

Supplementary information The online version contains supplementary material available at https://doi.org/10.1038/s44161-022-00155-0.

Correspondence and requests for materials should be addressed to Sabine Steffens.

Peer review information *Nature Cardiovascular Research* thanks Claudia Monaco, Cherry Wainwright and Almudena Ramiro for their contribution to the peer review of this work.

https://doi.org/10.1038/s44161-022-00155-0

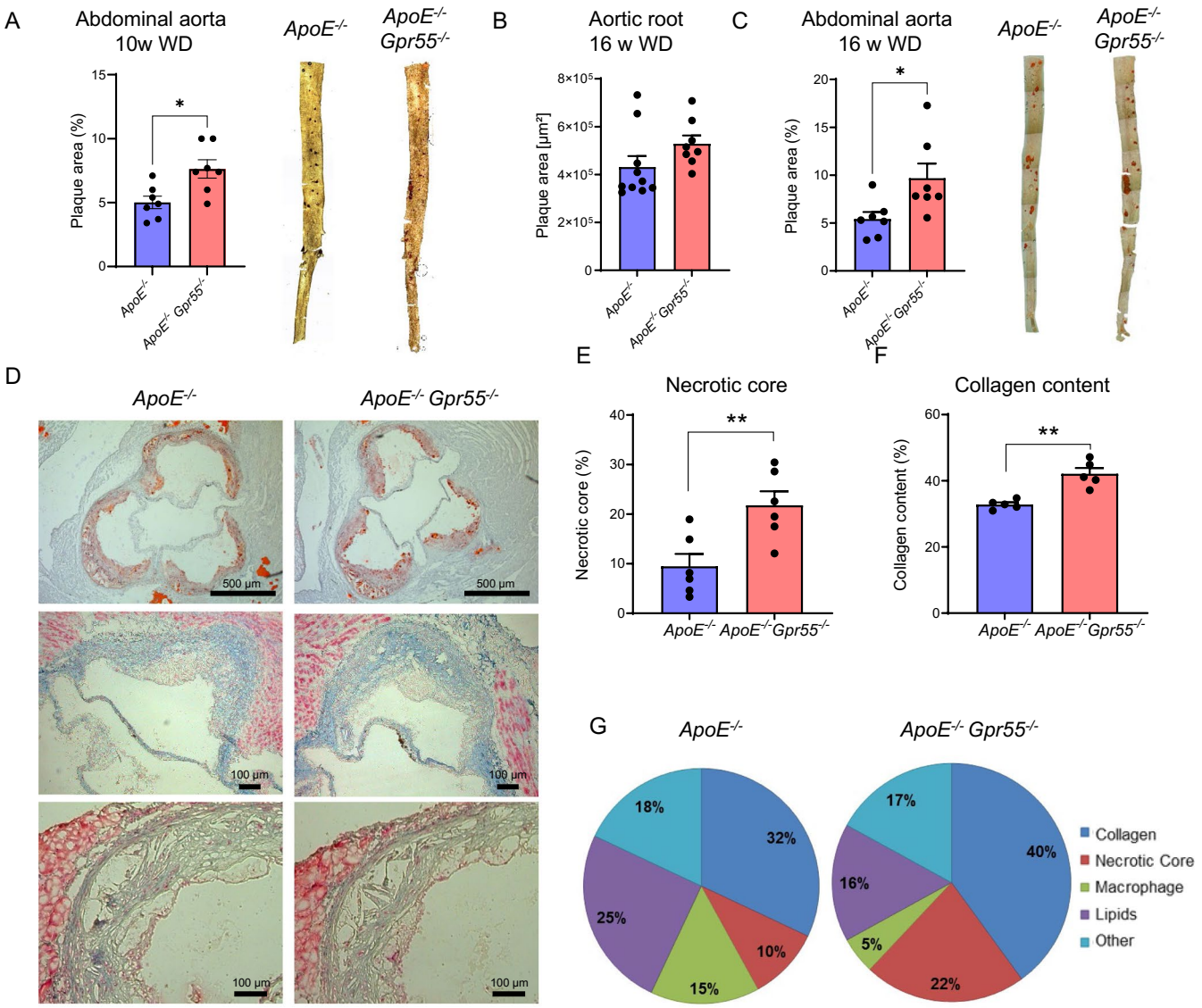

Extended Data Fig. 1 | Impact of global *Gpr55* deficiency on advanced stage of atherosclerosis. (**a**) Plaque area within descending thoraco-abdominal aortas after 10 weeks Western diet (WD) (n = 7; **P* = 0.011), determined by en face preparations stained with Oil-red-O, and calculated as percentage of plaque per total vessel area. (**b**) Aortic root average plaque area (calculated from sections 80–240 µm distance of the aortic root origin) after 16 weeks WD (n = 8–10). (**c**) Plaque area within descending thoraco-abdominal aortas after 16 weeks WD (n = 7; **P* = 0.027), determined by en face preparations stained with Oil Red O, and calculated as percentage of plaque per total vessel area. (**d**) Representative aortic root plaque images stained with Oil-red-O (upper) and Masson staining's (middle and lower images) for lipid or collagen content, respectively, and quantification of the necrotic core area after 16 weeks WD. (**e**) Necrotic core (n = 6; ***P* = 0.0086) and (**f**) collagen content per total plaque area (n = 6; ***P* = 0.0011) were calculated on 4 middle aortic root sections per mouse heart. (**g**) Relative plaque composition of main components in advanced plaques after 16 weeks WD. Data were combined from 3 independent experiments, each dot represent one biologically independent mouse sample (mean ± SEM). Two-sided unpaired Student's t-test was used to determine the significant differences ***P* < 0.01 vs the indicated group.

https://doi.org/10.1038/s44161-022-00155-0

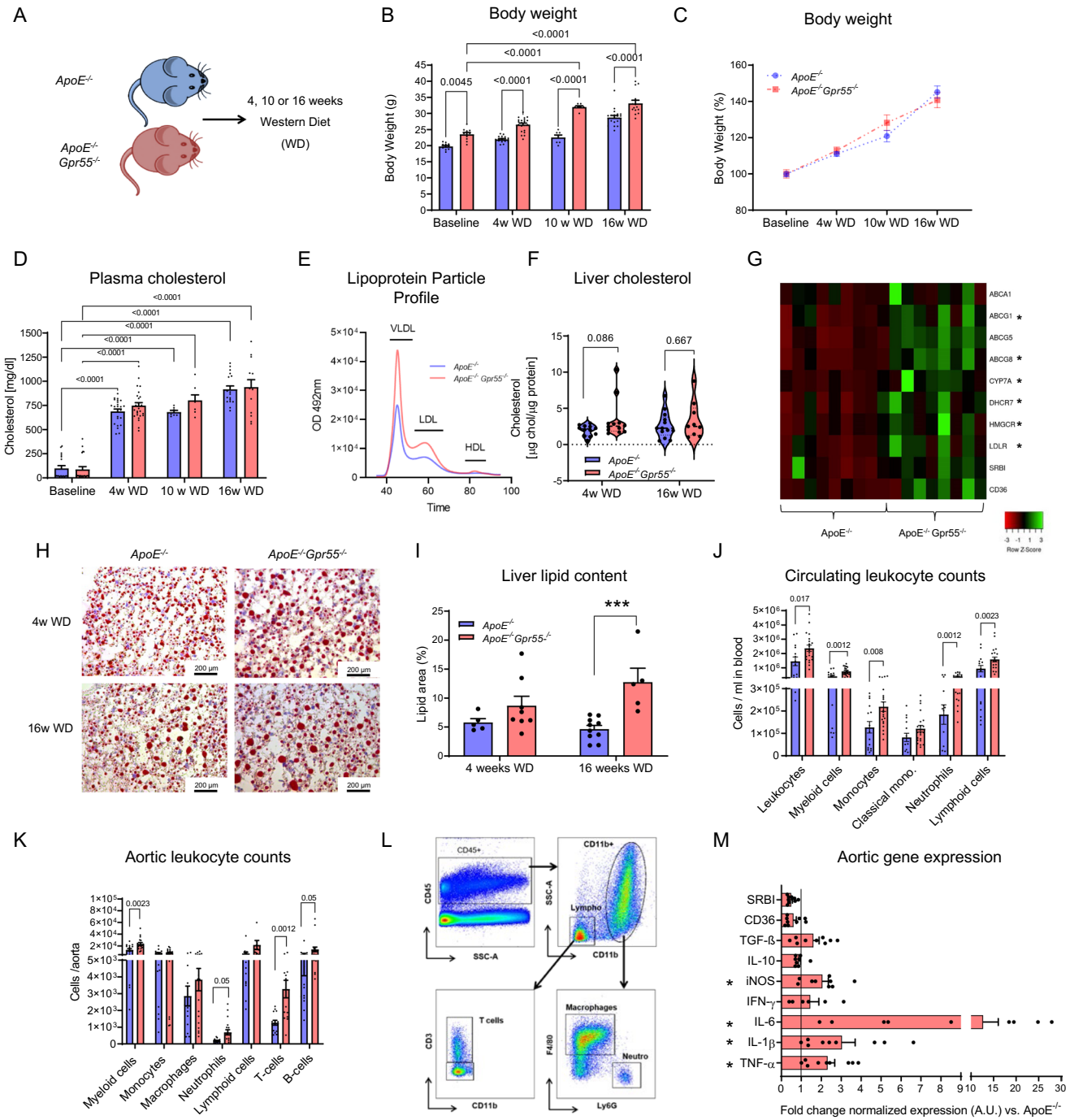

Extended Data Fig. 2 | Global *Gpr55* deficiency leads to increased metabolic dysfunction and inflammation during hypercholesterolemia. (**a**) Experimental scheme of the Western diet (WD) treatment and color code for Apoe−/− and Apoe−/−Gpr55−/− groups. For every panel, each dot represents a biologically independent mouse sample. (**b**) Average body weight of Apoe−/− vs Apoe−/−Gpr55−/− female mice (n = 12 for baseline, n = 14–18 for 4 and 16 weeks WD and n = 7–8 for 10 weeks WD) from different experimental end points (baseline, 4, 10 and 16 weeks WD); exact p values are shown in the panel figure. (**c**) The body weight gain per mouse was followed for the entire duration of a 16 weeks WD experiment, and calculated as percentage of the starting body weight (same animals that in panel B). (**d**) Total plasma cholesterol concentrations at baseline, 4, 10 and 16 weeks WD from Apoe−/− and Apoe−/−Gpr55−/− female mice; exact p values are shown in the panel. (**e**) Representative histograms of high-performance liquid chromatography separation of plasma lipoprotein fractions of Apoe−/− and Apoe−/−Gpr55−/− mice after 4 weeks WD (lines show the average of a pool of n = 3 per group). (**f**) Liver cholesterol concentrations, normalized to the total protein content per lysate, in Apoe−/− and Apoe−/−Gpr55−/− mice at 4 and 16 weeks WD; exact *P* values are shown in the panel. (**g**) Heatmap showing the relative liver mRNA expression of several genes involved in cholesterol metabolism for Apoe−/− vs Apoe−/−Gpr55−/−after 4 weeks WD. Each column represents one mouse (n = 8-9; $P < 0.05$). (**h**) Histological liver sections stained with Oil Red O for lipid droplet quantification (**i**), calculated per tissue area, after 4 and 16 weeks WD in Apoe−/− vs Apoe−/−Gpr55−/− mice; (n = 5–6; ***$P = 0.0007$). (**j**) Circulating leukocyte subsets per ml of blood in Apoe−/− vs Apoe−/−Gpr55−/− after 4 weeks WD were determined by flow cytometry; exact p values are shown in the panel (n = 10–12). (**k**) Aortic leukocyte subsets in Apoe−/− vs Apoe−/−Gpr55−/− mice after 4 weeks WD; exact *P* values are shown in the panel (n = 10–12). (**l**) Flow Cytometry gating strategy used for identification of aortic leukocyte subsets. (**m**) Aortic mRNA expression of representative key pro- and anti-inflammatory genes in Apoe−/− vs Apoe−/−Gpr55−/− mice after 4 weeks WD (n = 9–10; *$P < 0.05$). Data were combined from 2 independent experiments (mean ± SEM;). One-Way-ANOVA followed by a post-hoc Newman–Keuls multiple-comparison or two-way-ANOVA followed with Kruskal–Wallis test with Dunn post hoc test was used to evaluate the significant differences.

https://doi.org/10.1038/s44161-022-00155-0

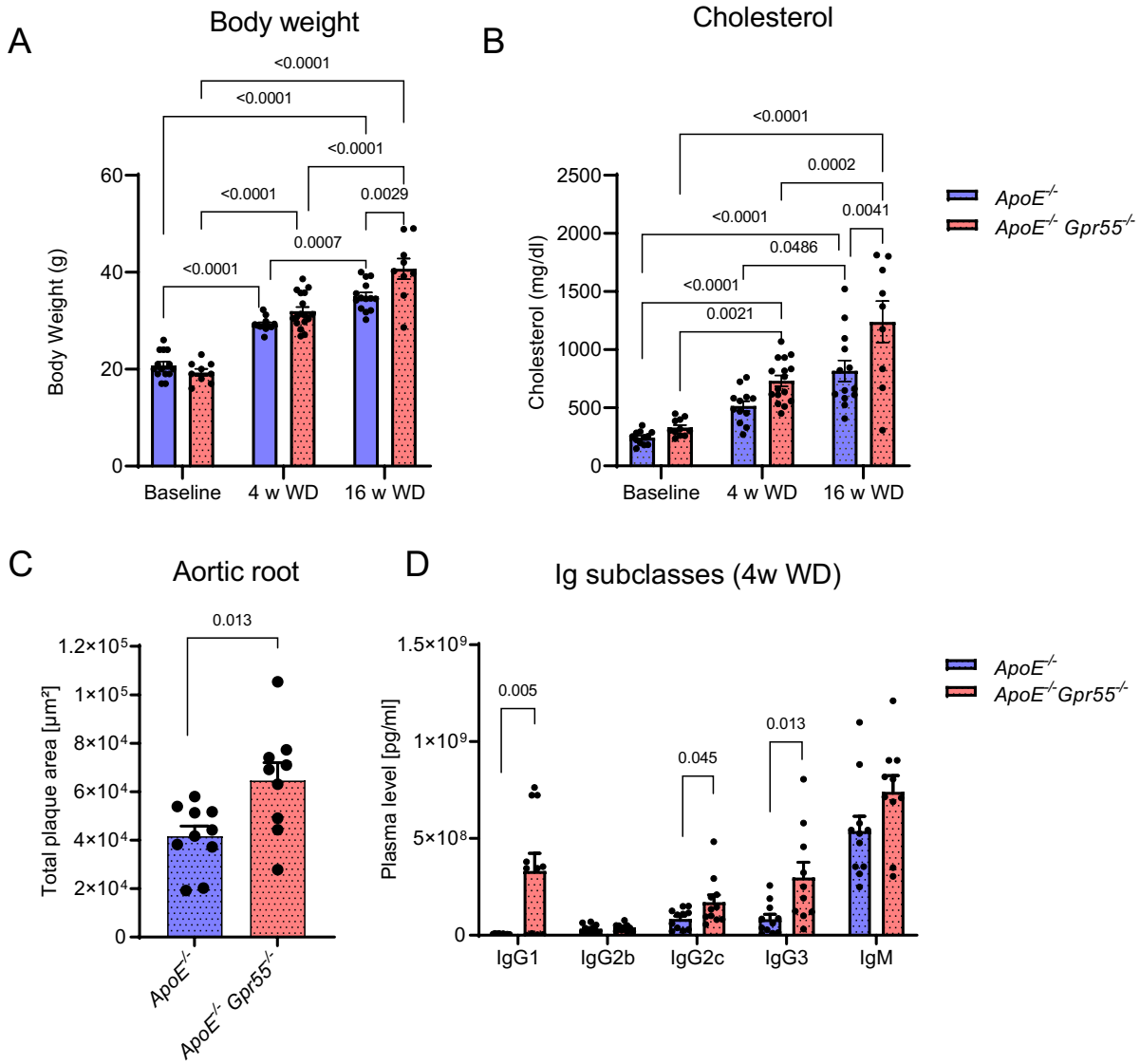

Extended Data Fig. 3 | Effects of global *Gpr55* deficiency on atherosclerosis in male mice. (**a**) Average body weight of Apoe−/− vs Apoe−/−Gpr55−/− mice from different experimental end points (baseline, 4 or 16 weeks WD; n = 9–12). (**b**) Total plasma cholesterol concentrations at different time points (baseline, 4 weeks WD, and 16 weeks WD) from Apoe−/− and Apoe−/−Gpr55−/− mice (n = 9–12). (**c**) Average plaque area in Oil Red O-stained aortic root sections (calculated from sections 80–240 µm) after 4 weeks WD in mice (n = 9–10). (**d**) Plasma Ig titers after 4 weeks WD (n = 9–10). Data are represented as mean ± SEM. Two-sided unpaired Student's t-test or one-Way-ANOVA followed by a post-hoc Newman–Keuls multiple-comparison test was was used to determine the significant differences. Each dot represents one biologically independent mouse sample, and exact *P* values are shown in each panel.

https://doi.org/10.1038/s44161-022-00155-0

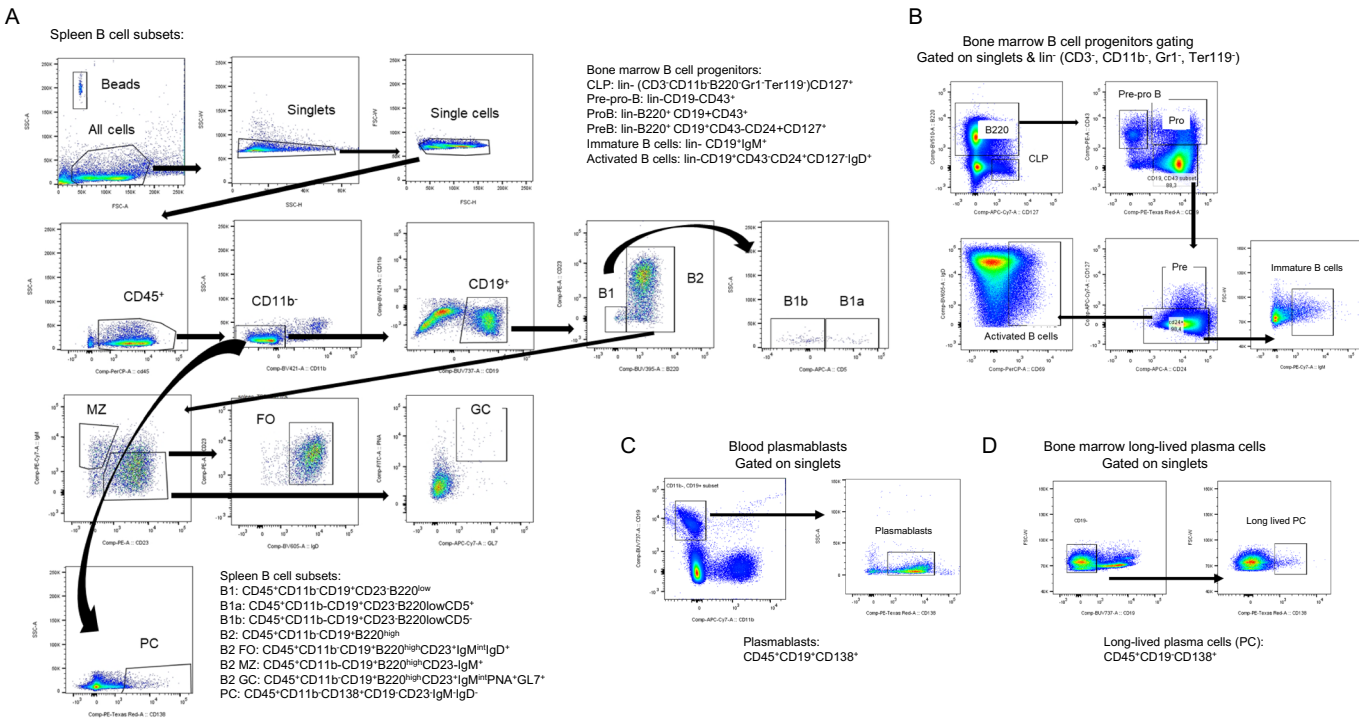

Extended Data Fig. 4 | Gating strategies. (**A**) Gating strategy used for determining the different splenic B cell subsets and list of subset markers used to identify each B cell population. (**B**) Gating strategy and list of markers used to identify the lymphoid and B cell progenitors in bone marrow and spleen. (**C**) Gating strategy for plasmablasts in blood. (**D**) Gating strategy for bone marrow long lived plasma cells (PCs).

https://doi.org/10.1038/s44161-022-00155-0

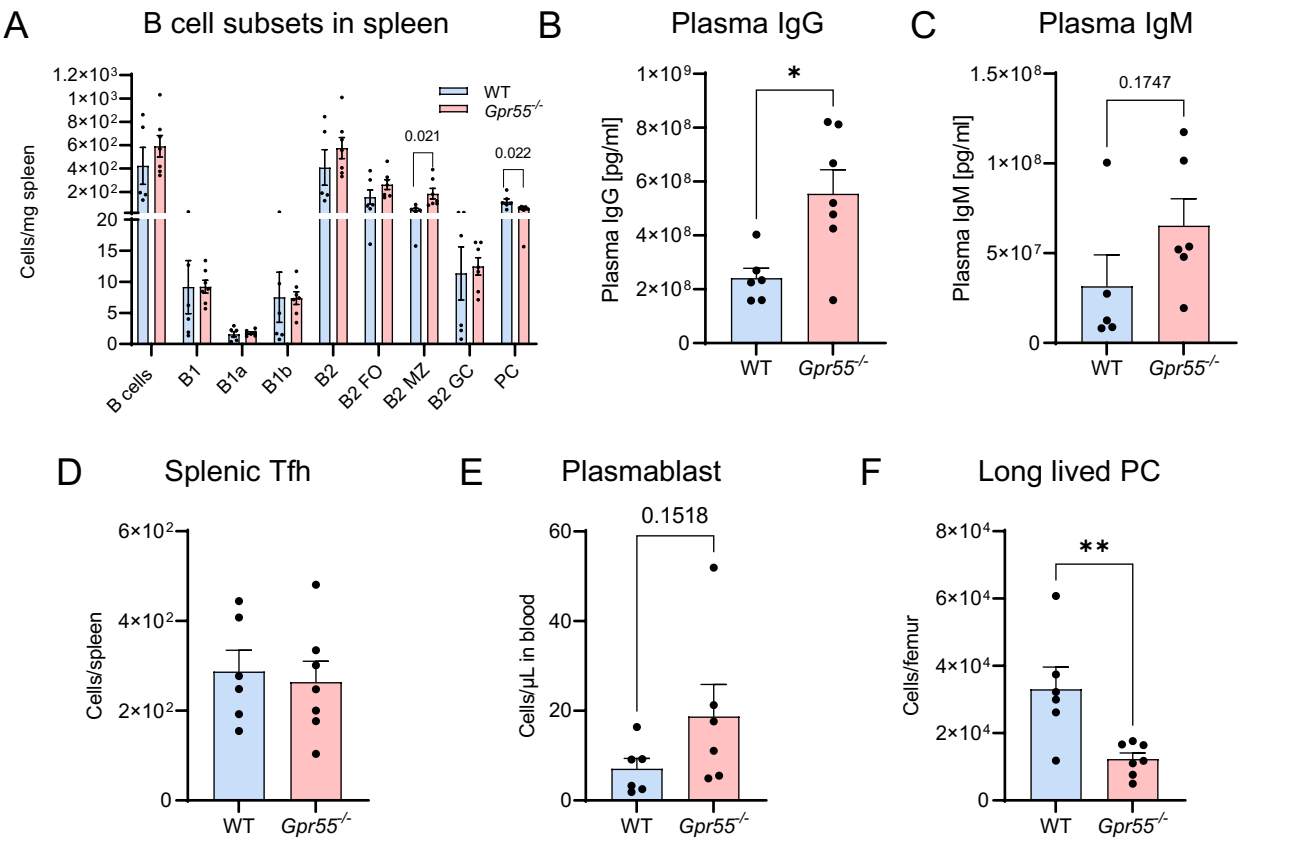

Extended Data Fig. 5 | B cell immunoprofiling in WT and *Gpr55*$^{-/-}$ mice on wild-type C57BL/6J background. (**a**) Flow cytometric quantification of splenic B cell subsets; exact *P* values are shown in each panel (n = 6–7). (**b**) Total plasma IgG (n = 6-7; *P* = 0.0107) and (**c**) IgM titers. (**d**) Number of splenic T follicular helper (Tfh) cells (n = 5–6), (**e**) circulating plasmablasts (n = 6–7) and (**f**) long lived plasma cells (LLPC) in bone marrow assessed by flow cytometry in 8 week old female WT and Gpr55−/− mice (n = 6–7; *P* = 0.0075). Data are mean ± SEM; each dot represents one biologically independent mouse sample. Two-sided unpaired Student's t-test was used to determine the significant differences. FO, follicular; GC, germinal center; MZ, marginal zone; PC, plasma cell; Tfh, T follicular helper cells; WT, wild-type.

https://doi.org/10.1038/s44161-022-00155-0

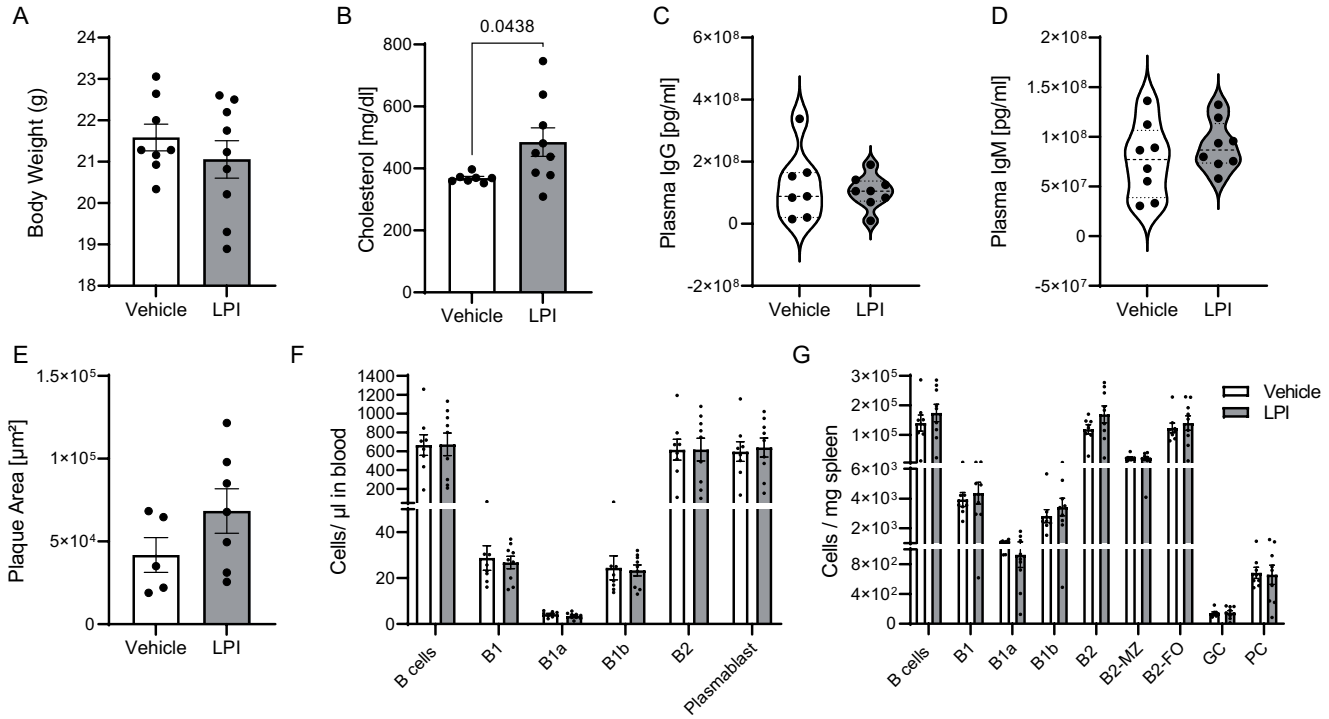

Extended Data Fig. 6 | Effects of lysophosphatidylinositol (LPI) treatment in parallel to 4 weeks Western Diet. Age- and weight-matched littermate female *Apoe*$^{-/-}$ mice were randomly divided into 2 groups to receive daily intraperitoneal injections of 0.1 mg/kg LPI or vehicle, respectively. Both groups were fed with Western diet for 4 weeks until endpoint analysis of (**a**) body weight (n = 8–9), (**b**) total plasma cholesterol (n = 7–9; $P = 0.0438$) as well as (**c**) total plasma IgG (n = 7–9) and (**d**) IgM titers (n = 7–9). (**e**) Average plaque area per aortic root cross-section (n = 5–7). (**f**) Circulating leukocyte counts (n = 7–9) and (**g**) splenic B cell subsets were quantified by flow cytometry (n = 7–9). Mouse data shown in A-G were obtained in one independent experiment (mean ± SEM; each point represents one animal). Two-sided unpaired Student's t-test (panels a–b and e–g) and Mann Whitney (panel c and d) was used to determine the significant differences. FO, follicular; GC, germinal center; LPI, lysophosphatidylinositol; MZ, marginal zone; PC, plasma cell.

https://doi.org/10.1038/s44161-022-00155-0

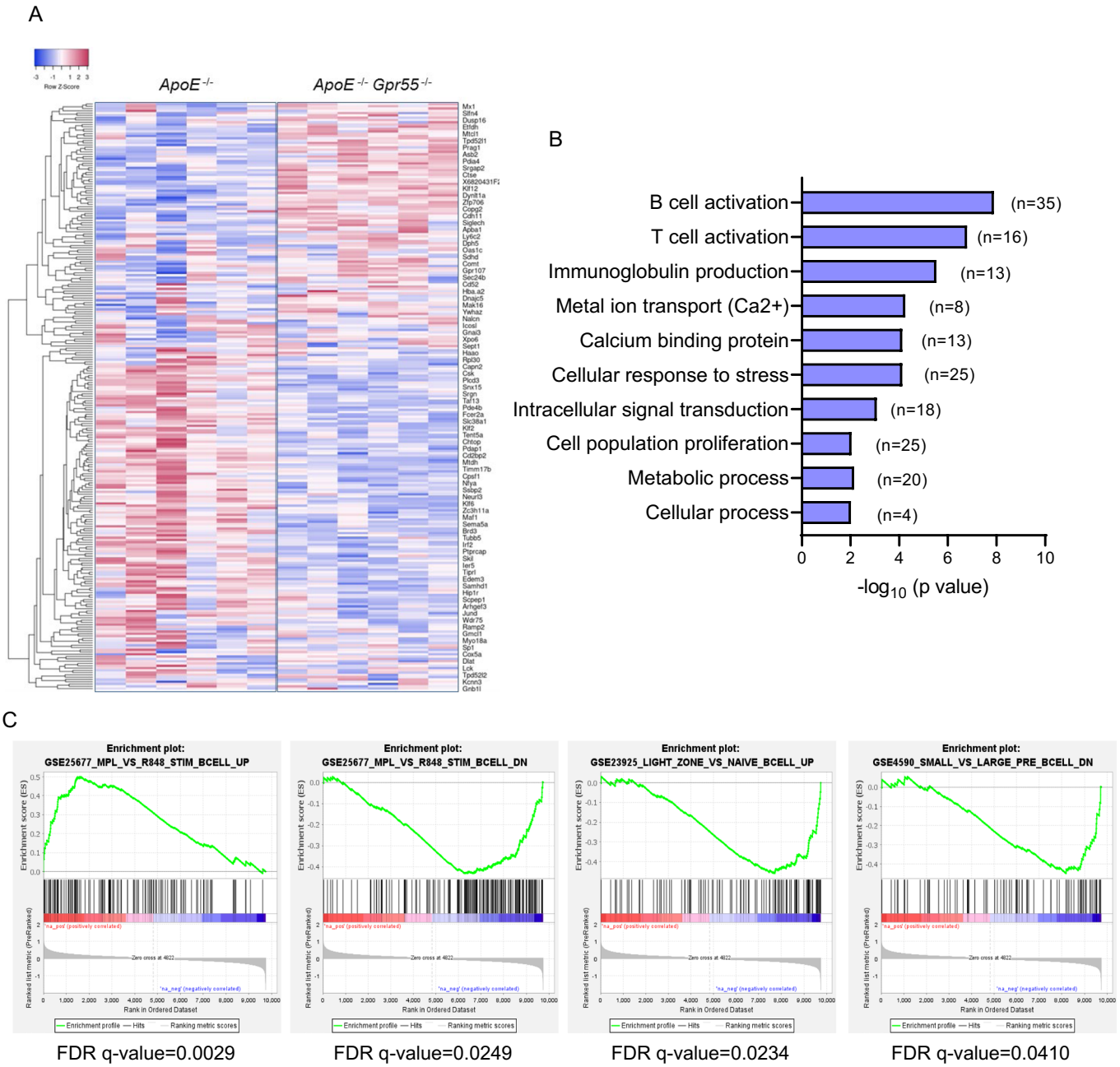

Extended Data Fig. 7 | RNA-sequencing of total splenic B cells from *Apoe*$^{-/-}$ vs *Apoe*$^{-/-}$*Gpr55*$^{-/-}$ mice. (**a**) Heatmap of the differentially expressed genes between splenic B cells (CD19+) isolated from Apoe−/− and Apoe−/−Gpr55−/− mice after for 4 weeks WD (adjusted *P* value 0.05, fold change ≥ $\log_2$ 1.5 fold change; n = 6). (**b**) Main regulated pathways based on gene ontology (GO) enrichment analysis, bars represent the *P* value significance; numbers in brackets indicate the number of genes regulated in each pathway. (**c**) Main molecular Signatures Database (MSigDB) annotated in the immunologic signature gene sets using GSEA software are shown; false discover rate (FDR) q-value for each enrichment plot is shown.

https://doi.org/10.1038/s44161-022-00155-0

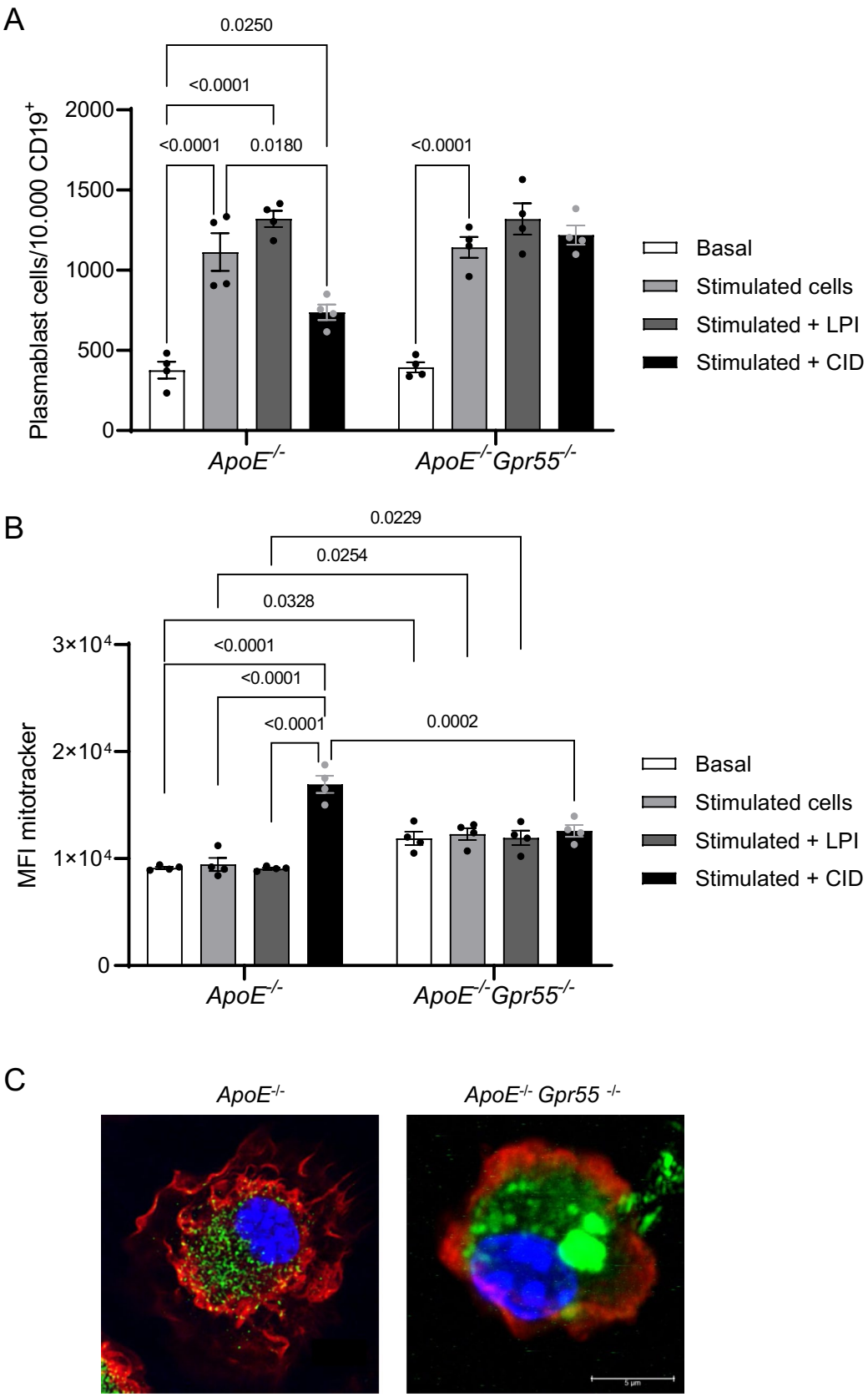

Extended Data Fig. 8 | See next page for caption.

https://doi.org/10.1038/s44161-022-00155-0

Extended Data Fig. 8 | Plasma B cell differentiation and characterization. (**A**, **B**) In vitro differentiation of splenic B cells into PCs alone or in presence of GPR55 ligand LPI or GPR55 antagonist CID16020046 using B cells isolated from baseline Apoe−/− or Apoe−/− Gpr55−/− female mice. After 7 days, PCs were quantified by flow cytometry gating for $CD45^{+}CD11b^{-}CD19^{+}$ $CD138^{+}$ cells (n = 4). (**B**) Mitochondrial content of differentiated PCs was determined by flow cytometry using Mitotracker, data are expressed as MFI (n = 4). (**C**) Representative confocal/STED images of differentiated PC from an Apoe−/− or Apoe−/−Gpr55−/− stained with Mitotracker (mitochondria, green), F-actin (red) and nuclei (blue); one representative picture of four biologically independent samples per group analyzed is shown, and 3 to 5 cells per sample were aquired. Two-way-ANOVA followed with Kruskal–Wallis test with Dunn post hoc.test was used to evaluate the significant differences; each dot represents one biologically independent mouse sample, and exact *P* values are shown in each panel (mean ± SEM).

https://doi.org/10.1038/s44161-022-00155-0

Extended Data Table 1 | Patient characteristics

	Stable plaque	Unstable/ruptured plaque
Number of patients	8	8
Age (median)	73	78
BMI (median)	26.2	26.4
Diabetes mellitus (absolute numbers)	2/8	1/8
Sex	2 female / 6 male	3 female / 5 male
Arterial hypertension (absolute numbers)	6/8	6/8
Coronary artery disease (absolute numbers)	4/4	4/4
Hyperlipidemia (absolute numbers)	6/8	7/8
Smoking	5/8	5/8
Symptomatic (stroke, TIA, amaurosis fugax; absolute numbers)	3/8	2/8

nature portfolio

Corresponding author(s): Sabine Steffens

Last updated by author(s): Sep 14, 2022

Reporting Summary

Nature Portfolio wishes to improve the reproducibility of the work that we publish. This form provides structure for consistency and transparency in reporting. For further information on Nature Portfolio policies, see our Editorial Policies and the Editorial Policy Checklist.

Statistics

For all statistical analyses, confirm that the following items are present in the figure legend, table legend, main text, or Methods section.

n/a	Confirmed	
☐	☒	The exact sample size (*n*) for each experimental group/condition, given as a discrete number and unit of measurement
☐	☒	A statement on whether measurements were taken from distinct samples or whether the same sample was measured repeatedly
☐	☒	The statistical test(s) used AND whether they are one- or two-sided *Only common tests should be described solely by name; describe more complex techniques in the Methods section.*
☐	☒	A description of all covariates tested
☐	☒	A description of any assumptions or corrections, such as tests of normality and adjustment for multiple comparisons
☐	☒	A full description of the statistical parameters including central tendency (e.g. means) or other basic estimates (e.g. regression coefficient) AND variation (e.g. standard deviation) or associated estimates of uncertainty (e.g. confidence intervals)
☐	☒	For null hypothesis testing, the test statistic (e.g. *F*, *t*, *r*) with confidence intervals, effect sizes, degrees of freedom and *P* value noted *Give P values as exact values whenever suitable.*
☒	☐	For Bayesian analysis, information on the choice of priors and Markov chain Monte Carlo settings
☒	☐	For hierarchical and complex designs, identification of the appropriate level for tests and full reporting of outcomes
☐	☒	Estimates of effect sizes (e.g. Cohen's *d*, Pearson's *r*), indicating how they were calculated

Our web collection on statistics for biologists contains articles on many of the points above.

Software and code

Policy information about availability of computer code

Data collection	We used the Microsoft Office package versions from 2016/2019/2021; for data flow cytometry analysis we used FlowJo v10.8.0 and v10.0.8. Data was plotted using GraphPad Prism 7 and 9.
Data analysis	Data was analyzed using GraphPad Prism 7 and 9 and Rstudio v1.4.1717 for RNA sequencing data analysis with DESeq2 library for analysis.

For manuscripts utilizing custom algorithms or software that are central to the research but not yet described in published literature, software must be made available to editors and reviewers. We strongly encourage code deposition in a community repository (e.g. GitHub). See the Nature Portfolio guidelines for submitting code & software for further information.

Data

Policy information about availability of data

All manuscripts must include a data availability statement. This statement should provide the following information, where applicable:

- Accession codes, unique identifiers, or web links for publicly available datasets
- A description of any restrictions on data availability
- For clinical datasets or third party data, please ensure that the statement adheres to our policy

RNA-sequencing data were uploaded in a public repository under GEO accession number GSE211594.

Field-specific reporting

Please select the one below that is the best fit for your research. If you are not sure, read the appropriate sections before making your selection.

☒ Life sciences ☐ Behavioural & social sciences ☐ Ecological, evolutionary & environmental sciences

For a reference copy of the document with all sections, see nature.com/documents/nr-reporting-summary-flat.pdf

Life sciences study design

All studies must disclose on these points even when the disclosure is negative.

Sample size	The sample size for experiments was estimated to achieve an a priori 85% statistical power for biologically significant differences (d=0.8) using a t distribution. We derived the data distribution (mean and standard deviation) of controls from literature and similar experiments performed in our laboratory. All the calculations were performed using G*Power v.3.1.9.
Data exclusions	To test for Gaussian distribution, D'Agostino Pearson omnibus or Shapiro–Wilk normality test was applied. Outliers were determined by Grubbs' test (alpha 0.05).
Replication	All the experiments were replicated at least two times and usually three times. The total number of individual samples (n) and independent experiments/batches that were combined are indicated in the figure legend for each data set.
Randomization	When necessary, the animals were listed and a number was assigned to the mice, then by using a software (http://www.randomizer.org) they were randomized in the different experimental groups.
Blinding	Investigators were blinded during sample acquisition and data analysis. All samples were assigned with a code and only after sample and data acquisition and data analysis the investigators knew to which group samples belong.

Reporting for specific materials, systems and methods

We require information from authors about some types of materials, experimental systems and methods used in many studies. Here, indicate whether each material, system or method listed is relevant to your study. If you are not sure if a list item applies to your research, read the appropriate section before selecting a response.

Materials & experimental systems

n/a	Involved in the study
☐	☒ Antibodies
☒	☐ Eukaryotic cell lines
☒	☐ Palaeontology and archaeology
☐	☒ Animals and other organisms
☐	☒ Human research participants
☒	☐ Clinical data
☒	☐ Dual use research of concern

Methods

n/a	Involved in the study
☒	☐ ChIP-seq
☐	☒ Flow cytometry
☒	☐ MRI-based neuroimaging

Antibodies

Antibodies used	We provided all information about the antibodies (antibody name, fluorochrome, brand, legend, clone and dilution) in the Extended Data table 1 .
Validation	We followed manufacturer's recommendation; for flow cytometry analyses the best antibody concentration was determined by calculating the stain index. For in vivo B cell depletion antibodies, previous studies were performed in our lab using these antibodies, in particular doses were tested to achieve at least 80% B cell depletion in the spleen.

Animals and other organisms

Policy information about studies involving animals; ARRIVE guidelines recommended for reporting animal research

Laboratory animals	Gpr55-/- mice on C57BL/6J wildtype (WT) background were purchased from the European Mouse Mutant Archive (EM:02355) and backcrossed with apolipoprotein E-deficient mice (ApoE−/−; strain # 002052, The Jackson Laboratory). Male and female ApoE-/- and ApoE-/-Gpr55-/- mice aged 7 to 9 weeks were used. Female Gpr55-/- mice aged 6-8 weeks were included for baseline plasma and immune cell measurements or isolation of bone marrow cells for transplantation. In other experiments, female Ldlr-/- mice (strain #:002207, The Jackson Laboratory), female Gpr55-/- mice on WT background and B cell-deficient (μMT) female mice (strain # 002288, The Jackson Laboratory) aged 6–8-weeks at the start of experimental regimes were used.

Wild animals	The study did not involve wild animals.
Field-collected samples	No field-collected samples.
Ethics oversight	All animal experiments were approved by the local Ethics committee of the District Government of Upper Bavaria (subject area 54 - veterinary matters) under the License Number: 55.2-1-54-2532-111-13 and 55.2-2532.Vet_ 02-18-114 and conducted in accordance with the institutional and national guidelines.

Note that full information on the approval of the study protocol must also be provided in the manuscript.

Human research participants

Policy information about studies involving human research participants

Population characteristics	Supplementary Table 4 describes the patient characteristics of the samples that have been used in this study.
Recruitment	Patient plaque samples were obtained from the Munich Vascular Biobank. Peripheral blood was obtained from healthy male and female volunteers (between 20 and 40 years old) to measure Ca2+ response to LPI for validation of GPR55 expression in human B cells.
Ethics oversight	The permission to collect human carotid atherosclerotic biospecimens for the Munich Vascular Biobank was approved by the local Hospital Ethics Committee (Ethikkommission der Fakultät für Medizin der Technischen Universität München, Munich, Germany). All patients provided their written informed consent. Blood sampling was approved by the Klinikum der Universität München ethics board (Ethikkommission), and participants gave written informed consent. The research involving human research participants have been performed in accordance with the Declaration of Helsinki.

Note that full information on the approval of the study protocol must also be provided in the manuscript.

Flow Cytometry

Plots

Confirm that:

☒ The axis labels state the marker and fluorochrome used (e.g. CD4-FITC).

☒ The axis scales are clearly visible. Include numbers along axes only for bottom left plot of group (a 'group' is an analysis of identical markers).

☒ All plots are contour plots with outliers or pseudocolor plots.

☒ A numerical value for number of cells or percentage (with statistics) is provided.

Methodology

Sample preparation	Splenic single cell suspensions were obtained by mashing the spleens through a 70-µm cell strainer. Femurs were centrifuged at 10,000 x g for 1 min after exposure of the distal metaphysis to collect the bone marrow cells. Splenic, bone marrow and blood erythrocytes were lysed with ammonium-chloride-potassium. For staining of leukocytes infiltrated into the aorta, the vessels were excised from the aortic arch to iliac bifurcation, and digested with collagenase IV and DNase I at 37° C at 750 rpm for 40 min and filtered through a 30-µm cell strainer. Blood, splenic, bone marrow, and aortic single cells were blocked for 5 min with Fc-CD16/CD32 antibody and then stained for 30 min in the dark at 4° C with antibodies.
Instrument	For flow cytometry:BD FACSCanto II flow cytometer (BD Biosciences) or Fortessa LSR (BD Biosciences).
Software	FlowJo v10.2 software (Tree Star, Inc).
Cell population abundance	Sorted fractions that were send for sequencing were 100% positive for the markers that we stated in the methodology section.
Gating strategy	The gating strategies are shown in Fig. 3, Extended Data Fig. 2 & 4.

☒ Tick this box to confirm that a figure exemplifying the gating strategy is provided in the Supplementary Information.